Article:

Liu, J, Liu, H, Wang, W et al. (11 more authors) (2018) First Results From the Ionospheric Extension of WACCM-X During the Deep Solar Minimum Year of 2008. Journal of Geophysical Research: Space Physics, 123 (2). pp. 1534-1553. ISSN 2169-9380

https://doi.org/10.1002/2017JA025010

First Results from the Ionospheric Extension of WACCM-X during the Deep Solar Minimum Year of 2008

Jing Liu[1], Hanli Liu[1], Wenbin Wang[1], Alan G. Burns[1], Qian Wu[1], Quan Gan[2], Stanley C. Solomon[1], Daniel R. Marsh[1], Liying Qian[1], Gang Lu[1], Nicholas M. Pedatella[1], Joe M. McInerney[1], James M. Russell III[3], and William S. Schreiner[4]

[1]High Altitude Observatory, National Center for Atmospheric Research, Boulder, Colorado, USA

[2]Department of Physics and Astronomy, Clemson University, Clemson, SC, USA

[3]Hampton University, Hampton, Virginia, USA

[4]COSMIC Program Office, University Corporation for Atmospheric Research, Boulder, Colorado

Corresponding author: Jing Liu (jingliu@ucar.edu)

Short Title: WACCM-X Simulated Ionosphere

Abstract

New ionosphere and electrodynamics modules have been incorporated in the thermosphere and ionosphere eXtension of the Whole Atmosphere Community Climate Model (WACCM-X), in order to self-consistently simulate the coupled atmosphere-ionosphere system. The first specified dynamics WACCM-X v.2.0 results are compared with several datasets, and with the Thermosphere-Ionosphere-Electrodynamics General Circulation Model (TIE-GCM), during the deep solar minimum year. Comparisons with Thermosphere Ionosphere Mesosphere Energetics and Dynamics satellite of temperature and zonal wind in the lower thermosphere show that WACCM-X reproduces the seasonal variability of tides remarkably well, including the migrating diurnal and semidiurnal components, and the non-migrating diurnal eastward propagating zonal wavenumber 3 component. There is overall agreement between WACCM-X, TIE-GCM, and vertical drifts observed by the Communication/Navigation Outage Forecast System (C/NOFS) satellite over the magnetic equator, but apparent discrepancies also exist. Both model results are dominated by diurnal variations while C/NOFS observed vertical plasma drifts exhibit strong temporal variations. The climatological features of ionospheric peak densities and heights (NmF_2 and hmF_2) from WACCM-X are in general agreement with the results derived from Constellation Observing System for Meteorology, Ionosphere and Climate (COSMIC) data, although the WACCM-X predicted NmF_2 values are smaller, and the equatorial ionization anomaly crests are closer to the magnetic equator compared to COSMIC and ionosonde observations. This may result from the excessive mixing in the lower thermosphere due to the gravity wave parameterization. These data-model comparisons demonstrate that WACCM-X can capture the dynamic behavior of the coupled atmosphere and ionosphere in a climatological sense.

1. Introduction

Capturing lower atmosphere forcing effects on the upper atmosphere is critical for predicting ionosphere and thermosphere states because of the intimate coupling between the lower and upper atmospheres. An earlier approach was to couple different models covering different domains [e.g., Liu and Roble, 2002; Hagan et al., 2007]. This produces artificial interfaces or boundaries and introduces unrealistic physical processes. In recent years, several whole atmosphere models have been developed that cover the whole Earth's atmosphere domain. Miyoshi and Fujiwara [2003] constructed the General Circulation Model (GCM), which extends from the ground to the exobase. Later, this model was updated to the coupled Ground-to-topside model of Atmosphere and Ionosphere for Aeronomy (GAIA), including the neutral atmosphere from the troposphere to the thermosphere, thermosphere-ionosphere coupling, and electrodynamics [Jin et al., 2011]. The Whole Atmosphere Model (WAM) [Akmaev et al., 2008; Fuller-Rowell et al., 2008], currently under development, is based on the National Weather Service operational Global Forecast System model covering altitudes from the ground to ~ 600 km. A thermosphere extension of the Whole Atmosphere Community Climate Model (WACCM-X) also began its development several years ago [Liu et al., 2010].

The usage of a whole atmosphere model has the following advantages [Roble, 2000]: (1) treatment of the lower atmosphere and the upper atmosphere as a completely coupled system in terms of physics, dynamics, and chemistry; (2) clarification of the possible two-way interactions between climate change in the upper atmosphere and lower atmosphere variability; (3) description of the climate response due to solar variability, possibly through changes in middle and upper atmosphere chemistry and dynamics; (4) a more accurate specification of shorter timescale changes in the thermosphere and ionosphere. A comprehensive review of the whole atmosphere modeling efforts was given by Akmaev [2011].

The ionosphere exhibits salient day-to-day variability due to lower atmosphere forcing, geomagnetic forcing, and solar radiation changes. During geomagnetically quiet periods, ionospheric day-to-day variability can be significantly impacted by lower atmospheric forcing, especially by the variability of atmospheric waves [e.g. Forbes et al., 1993;

Lastovicka, 2006; Kazimirovsky and Vergasova, 2009; Liu, 2016 and references therein]. Tides can be generated in different altitudinal regions due to the following processes: tropospheric latent heating, absorption of tropospheric infrared radiation by water vapor, absorption of solar ultraviolet radiation by stratospheric ozone, thermosphere molecular oxygen absorption of extreme ultraviolet radiation, and wave-wave interactions [Chapman and Lindzen 1970; Hagan and Forbes, 2002; Liu, 2016]. There are two schools of thoughts regarding the modulation of the ionosphere by tides: direct propagation of atmospheric tides into the ionosphere and thermosphere [e.g., Oberheide et al., 2009] and indirect coupling via the ionosphere E-region dynamo [e.g., Jin et al., 2008; Ren et al., 2010; Wan et al., 2012]. The former denotes direct penetration of certain tidal modes from the troposphere to the thermosphere, serving as an in situ source [Hagan et al., 2007]. The latter refers to the tides producing variations in the E-region winds, which modify the E-region dynamo. For instance, longitudinal variations of latent heating in the troposphere can excite non-migrating tides in the lower atmosphere, which can propagate upward and modify the wind in the MLT region [e.g., Immel et al., 2006; Wan et al., 2012]. The winds in the lower thermosphere cause the E-region polarization electric fields due to the differential motion between the ions and electrons. E-region dynamo electric fields then map along magnetic field lines into the ionosphere F-region ionosphere. Daytime eastward electric fields have great impacts on the latitudinal distribution of low-latitude ionospheric electron density by modifying the F-region ionospheric “fountain” effect.

Aside the aforementioned ionospheric dynamic effects, thermospheric composition and thus ionospheric electron density can also be affected by lower atmospheric wave forcing [e.g., Yue and Wang, 2014]. Seasonal variability of lower atmosphere tides is thought to be one of the potential causes of similar ionosphere variations. Tides can modify the upward propagation of gravity waves and their momentum deposition in the MLT region. Gravity wave breaking, having a strong seasonal dependence, changes the eddy diffusion in the lower thermosphere. This eddy diffusion has a tendency to transport O from the lower thermosphere downward and molecular species upward, leading to a composition change in the lower thermosphere. This effect is transmitted to higher altitudes through molecular diffusion and vertical advection of neutral species in the thermosphere [e.g., Akmaev and Shved, 1980; Forbes et al., 1993; Qian et al., 2009; Yamazaki et al., 2013; Yue and Wang, 2014; Burns et al., 2015]. Therefore, stronger eddy diffusion reduces the thermospheric O/N_2 ratio and ionospheric F-region electron densities, as these two parameters are positively correlated near the ionospheric F_2 peak height.

Most recently, ionospheric and electrodynamic modules have been incorporated in WACCM-X, allowing us to self-consistently simulate the whole atmosphere from the troposphere to the topside ionosphere without introducing any artificial interfaces between the different layers of the atmosphere. The objective of this paper is to evaluate this model by examining the first simulation results of this new version of WACCM-X through comparisons of the modeled electron density, vertical ion drifts, and tidal variability with multiple data sources, as well as with the Thermosphere-Ionosphere-Electrodynamics General Circulation Model (TIE-GCM) simulation results. These comparisons have been performed for the deep solar minimum year 2008 when the upward propagating lower atmospheric waves were expected to have stronger influences on the upper atmosphere. A description of the numerical models and data used for this study are given in the next section. Model-data comparisons are described in section 3. Section 4 discusses the relevance of these results as related to observations. Conclusions are given in section 5.

2. Model and Data Descriptions

2.1 WACCM-X Introduction

A detailed description of the new version (version 2.0) of WACCM-X (referred to as WACCM-X v.2.0) can be found in Liu et al. [2018]. A brief summary is given here: WACCM-X is an atmospheric component of the National Center for Atmospheric Research (NCAR) Community Earth System Model (CESM), which couples atmosphere, ocean, land surface, sea and land ice, and carbon cycle components through exchanging fluxes and state information [Hurrell et al., 2013]. It is based on the community atmosphere model (CAM) and Whole Atmosphere Community Climate Model (WACCM). The first version of WACCM-X was described by Liu et al. [2010]. Key developments and improvements of thermosphere and ionosphere modules in WACCM-X v.2.0 include:

1. Improvements of the momentum equation and energy equation solvers to account for the species dependence of atmosphere mean mass and specific heats.
2. A new divergence-damping scheme that reduces unrealistic damping of atmospheric tides.
3. Cooling by $O(^3P)$ fine structure emission.
4. A self-consistent electrodynamics module that solves the ionospheric electric potential driven by the neutral wind dynamo.
5. A module that solves the transport of O^+ in the F-region.
6. A time-dependent solver for electron and ion temperatures, and together with thermospheric heating due to thermal electrons.
7. Metastable O^+ chemistry and energetics.
8. Solar EUV ionization and heating that can accommodate solar spectra from high-time-resolution models or measurements.
9. Specification of auroral inputs.

The top boundary of WACCM-X v.2.0 is set at $4.0\text{x}10^{-10}$ hPa (~500 to ~700km altitude, depending on solar activity). The vertical resolution in the mesosphere and thermosphere is a quarter of a scale-height, and the horizontal resolution is 1.9^o x 2.5^o in latitude and longitude, respectively. WACCM-X has the option to have the tropospheric and stratospheric dynamics constrained to meteorological reanalysis fields for specifically targeted time periods. All WACCM-X results used in the paper are from a specified dynamics simulation of WACCMX, which is constrained up to 50 km by nudging towards the National Aeronautics and Space Administration (NASA) Modern-Era Retrospective Analysis for Research and Applications [Rienecker et al., 2011].

2.2 TIE-GCM v.2.0

The TIE-GCM is a community model developed at the NCAR High Altitude Observatory. It is a first-principles, upper atmosphere, general circulation model that solves the Eulerian continuity, momentum, and energy equations for the coupled thermosphere/ionosphere system, covering the altitude range from approximately 97 km to 600 km and having a horizontal resolution of $2.5° \times 2.5°$ and a vertical resolution of

1/4 pressure scale height [Roble et al., 1988; Richmond et al. 1992; Qian et al., 2012]. The main external drivers of the TIE-GCM are solar irradiance in the extreme-ultraviolet and far-ultraviolet spectral regions, geomagnetic activity forcing including auroral particle precipitation and ionospheric convection, and perturbation at the lower boundary of the model by tides/waves. The tidal forcing at the height of the lower boundary (~97 km) is specified by GSWM diurnal and semidiurnal migrating and non-migrating tidal amplitudes and phases [Hagan and Forbes, 2003].

TIE-GCM v.2.0 includes the following new physical features [Qian et al., 2014; Maute, 2017]: 2.5^{o} horizontal resolution is supported; electrodynamo calculations are parallelized; helium is calculated as a major species [Sutton et al., 2015]; argon is calculated as a minor species; the geomagnetic field is updated to the International Geomagnetic Reference Field version 12, and its annual secular variation is included for the years 1900-2020.

2.3 COSMIC Electron Density

The Constellation Observing System for Meteorology Ionosphere and Climate (COSMIC)/Formosat Satellite 3, a joint US/Taiwan radio occultation mission consisting of six identical micro-satellites, were launched on 15 April 2006, and have provided more than 4.4 million GPS radio occultation profiles to date. The ionospheric electron density maps presented in this paper are obtained from the radio occultation Abel inversion [Schreiner et al., 1999]. The Abel retrievals can cause systematic errors below the F layer in regions where horizontal electron density gradients are large but give a good estimation of the electron density in and above the F region, as well as peak electron density (NmF_2) and peak height (hmF_2) [e.g., Lei et al., 2007; Yue et al., 2010]. A Chapman α function was used to fit the ionospheric electron density profile between 170 and 600 km to derive NmF_2 and hmF_2 [e.g., Liu et al., 2009].

2.4 SABER Temperature and TIDI Winds

The Sounding of the Atmosphere using Broadband Emission Radiometry (SABER) instrument was launched onboard the Thermosphere Ionosphere Mesosphere Energetics Dynamics (TIMED) satellite on December 7, 2001. SABER measures the kinetic temperature from CO_2 emission within the altitude range of 20-120 km and extends from about 53° latitude in one hemisphere to 83° in the other. This viewing geometry alternates and has complete local time coverage every 60 days. Local Thermodynamic Equilibrium (LTE) and non-LTE retrieval algorithms are used, respectively, at altitudes below 70 km and in the upper MLT region [Mertens et al. 2004]. As mentioned by Remsberg et al. (2008), the random error in temperature data is less than 2 K below 70 km, and the error increases with altitude from 1.8 K at 80 km to 6.7 K at 100 km.

The TIMED Doppler Interferometer (TIDI) instrument on board TIMED provides global horizontal winds from 70-120 km with a vertical resolution of 2 km using a limb-scan Fabry-Perot interferometer. TIDI zonal winds in the MLT region are derived from Doppler shift measurements of green line emissions. NCAR-processed $O_2(^1\Sigma)$ atmospheric band (0–0) P9 line (763.51 nm) TIDI data (version 0307) with a new zero wind implementation were used for the current analysis [Killeen et al., 2006; Wu et al., 2008]. We performed a space-time series spectral analysis to the southern and northern tracks from a 60-d window separately, to obtain tidal amplitudes and phases of migrating and non-migrating tides.

3. Results

3.1 Ionospheric hmF_2 and NmF_2 Comparisons

Figure 1 shows the monthly median hmF_2 comparison between WACCM-X (left column), COSMIC (middle column), and TIE-GCM (right column) at March Equinox. The white dotted line denotes the dip equator. In general, the monthly median hmF_2 exhibits obvious diurnal variation and this diurnal variation has a clear latitudinal dependence. For instance, at middle latitudes, ionospheric hmF_2 is higher during nighttime than during daytime. Nighttime hmF_2 at middle latitudes is slightly underestimated by WACCM-X. Over the dip equator, daytime eastward dynamo electric fields produce upward ion drifts and are very effective at elevating the equatorial ionosphere to higher altitudes. That is why hmF_2 peaks around the equator on the dayside. This feature is well represented by WACCM-X and TIEGCM. Another noteworthy feature is that the global pattern of hmF_2 has a clear UT/longitude dependence, arising from the effects of, the offsets between geomagnetic and geographic poles, magnetic field declination, and non-migrating tides [e.g., Immel et al., 2006; Wan et al., 2012; Zhang et al., 2013; Liu et al., 2017].

Figure 2 is similar to Figure 1 but for June solstice. Apparently, daytime equatorial hmF_2 peaks move northward a little bit compared to those at March Equinox. In addition, nighttime middle latitude hmF_2 exhibits hemispheric asymmetry and hmF_2 in the summer hemisphere is higher than that in the winter hemisphere. This feature is well captured by WACCM-X and TIEGCM. This asymmetry is probably due to the mean summer-to-winter neutral flow and temperature effects. Mean summer-to-winter winds push the ionosphere upward in the upwind hemisphere (summer hemisphere) and press the ionosphere downward in the downwind hemisphere (winter hemisphere). In addition, stronger thermal expansion in the summer hemisphere also uplifts the ionosphere to higher altitudes, augmenting this seasonal asymmetry.

Figure 3 illustrates the monthly median NmF_2 comparisons between WACCM-X (left column), COSMIC (middle column), and TIE-GCM (right column) at March Equinox. NmF_2 is well arranged in geomagnetic coordinates. The low latitude equatorial ionization anomaly (EIA) is characterized by a minimum around the dip equator and two peaks around $\pm 15^o$ geomagnetic latitudes. In general, WACCM-X daytime NmF_2 is smaller at low latitudes than COSMIC and TIE-GCM. In addition, the two crests of the EIA from WACCM-X are closer to the dip equator than those in COSMIC data and TIE-GCM. The latitudinal separation of the two EIA peaks of both WACCM-X and COSMIC varies with universal time. The largest latitude distances between the two EIA crests are 32^o (WACCM-X) and 39^o (COSMIC) at 00 UT, 32^o (WACCM-X) and 45^o (COSMIC) at 06 UT, 26^o (WACCM-X) and 29^o (COSMIC) at 12 UT, and 32^o (WACCM-X) and 39^o (COSMIC) at 18 UT.

Figure 4 is similar to Figure 3 with a different color scale but at June solstice. Compared to NmF_2 at March equinox, there is an overall NmF_2 reduction at June solstice, which is characteristic of the semi-annual variation in ionospheric electron density [e.g., Burns et al., 2012; Qian et al., 2013]. At most UTs (0000, 0600, 1200 UT), the COSMIC data shows that the EIA crest in the winter hemisphere is stronger than that in the summer hemisphere from morning to noon; however, from noon to early afternoon, the winter EIA crest is weakened, and the crest in the summer hemisphere is intensified. Similar

EIA winter-summer asymmetry has been reported in the published literature and has been explained by the relative contributions from electrodynamics, thermodynamics, and chemical processes [e.g., Lin et al., 2007]. The simulated EIA features calculated by the two models somewhat differ from the COSMIC observations. At 0000 UT (first panels), for instance, COSMIC NmF_2 is weaker in the winter (south) crest than it in the summer (north) one in the longitude range from -180^o to -120^o, whereas both WACCM-X and TIE-GCM NmF_2 exhibit different characteristics, namely, the Southern EIA crest is stronger than the Northern crest within the longitude range from -180^o to -120^o. At 0600 and 1200 UT, this transition is roughly captured by WACCM-X and TIE-GCM. At 1800 UT, COSMIC NmF_2 is generally stronger in the Northern EIA crest than the Southern EIA crest, while WACCM-X simulated EIA crest is stronger in the South.

Detailed comparisons between WACCM-X and ionosonde observations are shown in Figures 5 and 6. Figure 5 gives hourly ionosonde-observed (black line) and WACCM-X (red line) (a) NmF_2 and (c) hmF_2 over Jicamarca (12°S, 283°W, 1°N geomagnetic latitude) during days 300-320 in 2008. Scatter plots between hourly observations and WACCM-X of (b) NmF_2 and (d) hmF_2 are for days 60-366 of year 2008. Both the model and observations exhibit salient day-to-day variability. An obvious feature in Figure 5a is the dramatic daytime NmF_2 enhancement around DOY 314. This could be related to the effects of recurrent geomagnetic storms generated by solar wind high-speed streams [e.g., Liu et al., 2012]. WACCM-X can generally capture the NmF_2 variability, but tends to underestimate the daytime NmF_2 by ~50%. Figure 5b also shows that the data are mostly located in the lower part of the plot, indicating systemically lower modeled NmF_2 values.

Figure 5c shows that equatorial hmF_2 is highly variable during this period (days 300–320) in both observations and model output. There is a reasonable agreement between WACCM-X and the observations in magnitude. The dots in Figure 5d are evenly distributed on both sides of the reference line. The highly variable hmF_2 over the equator shows that the electrodynamics processes undergo significant variability, probably caused by diurnal variations of lower atmospheric tide forcing, magnetospheric penetration electric fields and disturbed dynamo electric fields in association with recurrent geomagnetic storms [e.g., Liu et al., 2012]. The correlation coefficient is lower in Fig. 5d, probably related to the offset in temporal variations between data and model, whereas in

Fig. 5c, both are dominated by the comparatively larger diurnal variation of NmF_2, so the correlation is high.

Figure 6 is similar to Figure 5, but over Boulder (40.0^o N, 254.7^o W, 48.9^o geomagnetic latitude). Also, Figure 6a and 6c show ionosphere parameters during days 311–330 in 2008. This 11-day time shift between Figure 5 and Figure 6 is because there is large data gap over Boulder during days 300–320 in 2008. A bias still exists in NmF_2 for the whole year with the modeled NmF_2 values being about half of the observed ones in the daytime, as shown in Figure 6b. WACCM-X misses some spikes that are seen in observed hmF_2 (figure 6c). On the one hand, this simulation is driven by the low-resolution Kp index, which could miss prompt penetration electric fields effects or travelling atmosphere disturbances (TAD). Under the effects of penetration electric fields or TAD, the ionosphere can undergo dramatic elevation or depression depending on the direction of electric fields or TAD. On the other hand, this discrepancy could also represent problems with the spiky changes in hmF_2 observed by ionosondes during the nighttime.

Electric-field-induced vertical drifts have great impacts on the low-latitude ionospheric structure. Figure 7 compares the equatorial vertical drifts over Jicamarca with those from WACCM-X at 300 km (red solid line), TIE-GCM at 300 km (red dashed line), the Scherliess-Fejer (S-F) model (blue solid line), and the Communication/Navigation Outage Forecast System **(**C/NOFS) satellite. The Scherliess-Fejer model and C/NOFS vertical drift data were obtained from Stoneback et al. [2011]. Drifts from the Scherliess-Fejer model are based largely on Jicamarca radar and satellite datasets [Scherliess and Fejer, 1999]. C/NOFS data during the years of 2008–2009 within ±5^o magnetic latitudes and in the longitude range of 240^o–300^o E are binned according to season. In general, vertical drifts from these models are dominated by diurnal variations, whereas observations are characterized by strong temporal variations depending on the season. The three models (WACCM-X, TIE-GCM, and S-F model) exhibit similar features, with strong upward vertical drifts at local noon and weak or downward drifts in the evening. Large discrepancies still exist between these three models and C/NOFS. For example, WACCM-X tends to overestimate the downward drifts at around midnight for all four seasons. In March equinox, the three models fail to capture the C/NOFS observed downward drifts at around 1500 LT.

At March Equinox, this comparison highlights the presence of semi-diurnal or terdiurnal components of measured ion drifts, characterized by upward drifts in the post-midnight (0200-0400 LT), daytime (0800-1400 LT), and early night (1800-2300 LT). The postmidnight upward equatorial drifts may be related to thermospheric dynamics in association with the midnight temperature maximum [Stoneback et al., 2011; Fang et al., 2016]. There is an overall agreement between models and observations in capturing daytime upward drifts. However, all three models tend to underestimate the early night upward drifts and fail to capture the strong downward drifts with a magnitude of 50 m/s at around 0600 LT.

At June Solstice, the observed vertical drifts exhibit similar variations to those at the March equinox, but they are shifted to later local times by about 2 hours. The three models overestimated daytime drifts. Inconsistencies also exist in the post-midnight sector in which models predict downward drifts with a magnitude of 10 m/s, whereas the C/NOFS data show upward drifts.

At September Equinox, C/NOFS observed vertical drifts are less than 10 m/s and smaller than those of the 3 models. WACCM-X overestimates the downward drift in the post-midnight sector by about 10 m/s relative to the S-F model and TIE-GCM.

At December Solstice, C/NOFS observed vertical drifts are characterized by semi-diurnal variations and are upward at around 1000–1400 LT and 2000–0400 LT. The late morning and afternoon upward vertical drifts are prominent and well captured by models. The models, however, failed to reproduce the upward drifts in the nighttime sector (2000–0400 LT).

3.2 Tidal Comparisons

Tides play important roles in modulating the neutral wind dynamo in the lower thermosphere and the E-region ionosphere. The WACCM-X-simulated, migrating, diurnal, zonal wavenumber 1 (DW1, Figure 8) and semi-diurnal, zonal wavenumber 2 (SW2, Figure 9) tides, and non-migrating, eastward-propagating, diurnal tide with zonal wavenumber 3 (DE3, Figure 10) are compared with the TIMED satellite observations for

2008 in this section. Figure 8 compares the temperature (upper panels) and zonal wind (bottom panels) amplitudes of DW1 between WACCM-X (left columns) and observations (right columns) at March Equinox, when DW1 maximizes [e.g., Zhang et al., 2006; Gan et al., 2014]. Overall, for DW1, there is a good agreement between the WACCM-X simulations and TIMED measurements of zonal winds and temperatures in terms of spatial structure, with the primary peak located at the equator and between 95-105 km. The DW1 temperature amplitude from WACCM-X reaches 17.5–20 K, which is ~3–5 K lower than the DW1 amplitude from SABER data, though it agrees with the DW1 amplitude obtained from 2002-2006 SABER analysis [Akmaev et al., 2008]. The secondary peaks of ~10 K occur at around ±40^{o} S/N within the altitude range of 95–110 km for both WACCM-X and SABER. The DW1 zonal wind amplitude from WACCM-X has a similar spatial pattern to the TIDI DW1 zonal wind amplitude, with a maximum at around ±30^{o} and a larger amplitude in the southern hemisphere. The wave amplitude from WACCM-X, however, is weaker than that found in the TIDI analysis, with the WACCM-X peak amplitude in the southern hemisphere being ~30 m/s less than that from the TIDI data.

Figure 9 shows height versus geographic latitude distributions of the migrating semidiurnal tide (SW2) temperature and zonal wind amplitudes in July, when SW2 attains its largest magnitude. The temperature amplitude maxima from WACCM-X are located at latitudes near 30^{o} and altitudes of ~115 km in the NH and near -15^{o} at above 120 km in the SH. The summer hemisphere maximum (~50 K) is stronger than the winter one (~30 K), and the summer hemispheric amplitude at 110 km is slightly larger than that in the SABER data. The zonal wind amplitude maximizes at higher geographic latitudes (~50^{o}) and has the same summer-winter seasonal dependence. The peak summer hemispheric amplitude from the model (~55m/s) is weaker than that from the TIDI data (larger than 60m/s).

Figure 10 illustrates the cross-section of DE3 temperature and zonal wind amplitudes in July. There is also a general agreement in the spatial structures between WACCM-X and the TIMED data. The latitudinal structure of the DE3 tide above 100 km height is approximately symmetrical about 10^{o} S, but some contribution of the asymmetric DE3 tidal modes has been found below 95 km as well. SABER temperature amplitude tends to maximize at 105–118 km with amplitudes of 15–20 K, whereas DE3 in zonal winds attain their largest values at somewhat lower altitudes compared with those of the temperature. The peak DE3 temperature amplitude from WACCM-X is 8-10 K, weaker than the SABER analysis for 2008, although the DE3 amplitude agrees with the SABER DE3 analysis over 2002–2006 (at 116 km, Akmaev et al., 2008). The peak DE3 zonal wind amplitude from WACCM-X is ~10 m/s less than that from the TIDI DE3 analysis.

Figure 11 shows the seasonal variation of temperature amplitudes in DW1 (upper panel), DE3 (middle panel), and SW2 (lower panel) at 95, 110, and 105 km, respectively, for both WACCM-X (left column) and SABER (right column). Both WACCM-X and SABER show the distinctive signature of the first symmetric propagating component of DW1, namely a maximum at the equator and secondary maxima near ±35° latitudes. As seen in previous plots, the DW1 amplitude in WACCM-X temperatures (9–15 K) is less than that in SABER temperatures (15–18 K). The secondary peak from SABER is located at around ±35° geographic latitude, where the tidal amplitude reaches 6–9 K. The top panels indicate a strong semi-annual variation of DW1, with the maximum and minimum amplitudes during the equinoxes and solstices, respectively, in WACCM-X and SABER at 95 km. It is also evident that the maximum at the March equinox is larger than that at the September equinox. The DW1 variation has been well recorded by ground-based and satellite observations [e.g., McLandress et al., 1996; Zhang et al., 2006; Gan et al., 2014] and explained by either similar variation of heating sources [Hagan and Forbes, 2002; Lieberman et al., 2003], semi-annual variation of stratosphere and mesosphere background winds [Mclandress, 2002], or similar damping within the MLT region [Xu et al., 2009; Lieberman et al., 2010].

The SABER DE3 temperature amplitude is dominated by an annual variation. The SABER DE3 distribution is symmetric about 5°S latitude with maximum amplitudes (~18 K) between July and October, and minimum amplitudes between December and May. The WACCM-X amplitudes have a similar peak (~12 K) in September and minimize at around November. However, WACCCM-X predicts a secondary DE3 peak around January, which is much weaker in SABER observations.

The SW2 tide shows a clear semi-annual variation with maxima around the solstices. At the altitude examined here (105km), SABER SW2 has the strongest amplitude in

August and secondary peaks in December, and the northern and southern peaks are comparable. WACCM-X SW2, on the other hand, has peaks in the summer hemisphere and amplitudes at the two solstices are comparable. The temperature tide from WACCM-X is stronger in the NH (~ 18 K) than in the SH (~ 12 K), but these values are weaker than the temperature tidal amplitudes of the tides measured by SABER. It should be noted that the SW2 tide and its seasonal variation might change quite rapidly with altitude (and probably also inter-annually). For example, the SABER SW2 analysis for the time period of 2002–2006 display larger peaks in the winter hemisphere, and the peak values at the two solstices are comparable at 100 km [Akmaev et al., 2008]. Similar latitudinal/seasonal dependence is also seen in the SW2 zonal and meridional wind amplitudes at ~95 km in WACCM-X [Liu et al., 2018].

Seasonal variations of lower and middle atmosphere processes can modify thermospheric composition and electrodynamics, and thus contribute to the ionospheric seasonal variability. As shown in Figure 12, seasonal variations of the ionosphere are prominent both in the model and observations from the COSMIC satellites. The median of these NmF_2 values was calculated for all local solar times between 0900 and 1500 for all longitudes and 3-degree bins in magnetic latitude. Several noticeable features in the mid- and low-latitude ionosphere are seen in this plot. The most salient feature is that COSMIC NmF_2 has two peaks around equinoxes and exhibits equinoctial asymmetry with larger values at March Equinox. The WACCM-X NmF_2 has a similar semiannual variation even though WACCM-X tends to underestimate the NmF_2 at mid- and low-latitudes.

WACCM-X simulated hmF_2 is in reasonable agreement with that from COSMIC. Both COSMIC observations and WACCM-X simulations indicate that hmF_2 tends to maximize around the magnetic equator and has a preference for the summer side due to the effects of neutral winds and temperature [Rishbeth, 1998]. The discrepancy lies in that WACCM-X simulated hmF_2 is about 20–50 km higher in the equatorial regions of both hemispheres and about 20 km lower in the middle latitudes of the northern hemisphere.

4. Discussion

Comprehensive comparisons between WACCM-X and several datasets indicate that WACCM-X is able to capture realistic tides and ionospheric features. Quantitatively, however, apparent discrepancies between model results and observations also exist, indicating the need for further improvement of the model.

4.1 Equatorial Ionization Anomaly Model-Data Comparisons

One of the model-data discrepancies concerns the fact that the WACCM-X simulated EIA is weaker and closer to the equator than the EIA seen in COSMIC observations. It is well established that electric fields play important roles in shaping the EIA structure [Rishebeth, 2000]. In the presence of a near horizontal magnetic field, the EIA is formed by the eastward daytime electric field pushing plasma upward; this in turn affects ambipolar diffusion along field lines. The detailed comparison in Figure 7 illustrates that downward ion drifts from WACCM-X in the post-midnight sector are much stronger than those in the TIE-GCM and the S-F empirical model, as well as C/NOFS observations. Downward ion drifts reduce the electron density due to fast chemical reactions in the thermosphere-ionosphere system below the F_2 peak. The E-region dynamo is driven by poleward neutral winds in the thermosphere [see Heelis, 2004 and references therein]. Any process that can modulate either the winds or the electric fields that they create can modify the strength of the EIA. The tidal winds in the E-region ionosphere modulate the EIA through the E-region dynamo. This requires a more realistic tidal specification in the ionosphere electric dynamo region. It is anticipated that assimilating the lower atmosphere data into WACCM-X will capture more realistic tidal features [e.g., Pedatella et al., 2013].

Apart from electric fields, stronger ambipolar diffusion, lower O/N_2, and thermosphere winds could also be responsible for the overall reduction in WACCM-X simulated NmF_2 in the EIA region. Low O/N_2 in the thermosphere could be related to strong tidal or gravity wave dissipation in WACCM-X, leading to stronger eddy diffusion around the mesopause. A plausible cause of this discrepancy is then that the eddy diffusion from the current gravity wave parameterization scheme used in the model is too large and continues to grow with altitude till ~200 km. This eddy diffusion can transport O from the lower thermosphere downward and molecular species (N_2) upward, leading to a compositional change in the lower thermosphere. This effect will be transmitted to higher altitudes by vertical advection and molecular diffusion of neutral species in the thermosphere. Generally, because of a larger scale height of O than N_2, stronger eddy diffusion increases mixing and thus reduces the O/N_2 ratio [Forbes et al., 1993; Lastovicka, 2006; Kazimirovsky and Vergasova, 2009; Qian et al., 2009]. The O/N_2 ratio is positively correlated with electron density through production by solar EUV radiation and loss through recombination with the molecular neutral species. Sensitivity tests (not shown here) illustrate that turning off the eddy diffusion above the turbopause increases F region ionospheric electric density.

4.2 WACCM-X Simulated Seasonal Variations of Ionospheric NmF_2 and hmF_2

Figure 12 compares the daytime climatology of NmF_2 and hmF_2 observed by COSMIC and simulated by WACCM-X. COSMIC hmF_2 is generally dominated by an annual variation that peaks on the summer side of the magnetic equator. This is associated with the prevailing summer-to-winter mean flow (Figure 12), which raises the ionosphere in the upwind (summer) hemisphere and lowers the ionosphere in the downwind (winter) hemisphere. This prevailing summer-to-winter mean flow also drives an annual variation on O/N_2 and NmF_2 (Figure 12) at midlatitudes.

Daytime, low-latitude, ionospheric NmF_2 exhibits annual and semiannual variations, with maxima near equinoxes, a primary minimum at June solstice, and a secondary minimum in December solstice. These general features are captured by WACCM-X. Differences also occur. The model simulated NmF_2 semiannual variation is weaker than that measured by COSMIC. Another noticeable difference between WACCM-X results and COSMIC observations is that the model-simulated, seasonal peak of the northern EIA crest extends into January, whereas the observed one is confined near March. There is an offset in the month of the peak between the model and the data at September equinox maxima: in the observations the northern hemisphere peak occurs near October and the southern hemisphere one after October, whereas in the model simulations the northern hemispheric peak is offset towards the winter solstice but the southern one, which is much weaker, occurs near September.

There is no agreement yet on the cause of the semiannual variations of NmF_2, although it is clearly related to the semiannual variation in thermospheric composition.

Several mechanisms have been proposed to explain this phenomenon, including competing effects between O/N_2 changes caused by thermosphere circulation and solar zenith angle [e.g., Millward et al., 1996; Rishbeth, 1998], a more mixed thermosphere in solstice than in equinox caused by global-scale inter-hemispheric thermosphere circulation [e.g., Fuller-Rowell, 1998], eddy diffusion by gravity wave dissipation [e.g., Qian et al., 2009; 2013], and semi-annual variations of geomagnetic forcing [Cliver et al., 2000 and references therein].

It is worth mentioning that O/N_2 exhibits semiannual variations that maximize at the equinoxes and minimize at the solstices in the equatorial region (Figure 12). However, the peak-to-valley ratio of the semiannual components in WACCM-X O/N_2 over the magnetic equator is much weaker than that found by Qian et al., [2009] after adjusting the seasonal variation of eddy diffusion at the lower boundary of the TIE-GCM. The weak semi-annual variations in the simulated O/N_2 can lead to weaker seasonal variations in low-latitude NmF_2. This O/N_2 semiannual variation is mostly related to thermosphere circulation effects, which are caused by internal thermospheric dynamics [Fuller-Rowell, 1998] and mesosphere eddy diffusion [Qian et al., 2009]. Improper parameterization of seasonal variations of eddy diffusion caused by gravity waves could be one potential cause. The eddy diffusion coefficient Kzz is a product of the gravity wave parameterization in the model [Garcia et al., 2007; Richter et al. 2010]. In WACCM-X, the low-latitude Kzz value at 110 km peaks from May to October as shown in Figure 12. Increasing Kzz reduces the O/N_2 ratio and depletes electron density. Qian et al. [2013] compared the TIE-GCM runs with and without the seasonal variations of eddy diffusion at the lower boundary and showed that imposing seasonally variable eddy diffusion improves the comparison between the modeled and COSMIC-observed NmF_2. It should be noted that Kzz in WACCM-X represents the effects of sub-grid turbulent mixing. It is different from the TIE-GCM Kzz, which represents not only all sub-grid mixing processes that are not captured by the model, regardless of causes, but also the effects from all other lower and middle atmospheric processes that produce variability in vertical transport at and above the mesopause region where the model lower boundary is located [Qian et al., 2013; Qian et al., 2017]. Very limited observations related to eddy diffusion are available: those that are show that eddy diffusion is larger during the solstices than during the equinoxes, with stronger turbulence in summer than in winter [e.g., Kirchhoff and Clemesha, 1983; Fukao et al., 1994; Sasi and Vijayan, 2001]. This could be one of the potential causes of the discrepancy.

An additional source of the discrepancy between modeled and observed NmF_2 is the very weak seasonal variation of the modeled vertical drifts, as illustrated in Figure 12. Equatorial vertical drifts maximize at March equinox, with a magnitude of about 20 m/s and are similar in other months. However, previous studies demonstrated that equatorial vertical drifts exhibit a strong seasonal variation [e.g., Fejer et al., 2008; Su et al., 2008; Kil et al., 2009]. As shown in Figure 7 in Kil et al. [2009], the observed daytime vertical drifts show a strong semiannual variation, peaking at the equinoxes with magnitudes of ~22 m/s. The modeled vertical drifts are closer to the observed ones at March equinox, but are weaker than those at September Equinox. Lack of a semiannual variation in the vertical drifts modifies the seasonal variation of the daytime "fountain" effect, and thus modifies the seasonal variation of electron density correspondingly. This could be one of the potential causes of the discrepancy between WACCM-X and the data regarding the low latitude seasonal variation of NmF_2. But it is unclear to what degree such a weak semi-annual variation in vertical drifts can be responsible for the rather large difference in the seasonal variation of NmF_2 between the model and the observations.

Several possible mechanisms have been proposed to explain the semiannual variation, and there could be complex interactions among these processes. Further investigation is thus needed in future studies to explore the relative contribution of the above-mentioned processes, as well as other processes.

5. Conclusions

The first ground-to-space simulation results from WACCM-X with a self-consistent ionosphere and electrodynamics reveal a realistic representation of the seasonal variation of migrating and non-migrating tides, ionospheric electric fields induced vertical ion drifts, NmF_2, and hmF_2. Comparisons with observations from the TIMED satellite in the lower thermosphere show that WACCM-X reproduces the seasonal variability of tides remarkably well, including DW1, DE3, and SW2. Comparisons between WACCM-X and COSMIC ionospheric parameters show that WACCM-X can capture the ionosphere morphology during the deep solar minimum year of 2008 reasonably well. However, it should be noted that there is considerable evidence that the F-region ionosphere was, on average, as much as 10% lower in density during 2008–2009 than during previous solar minima, and that solar EUV radiation parameterized using the $F_{10.7}$ index cannot fully account for this effect [Solomon et al., 2013]. The WACCM-X and TIE-GCM runs performed for this study employed $F_{10.7}$ without any adjustment, so they should be expected to be slightly higher than COSMIC observations; instead of they are somewhat lower. Nevertheless, the detailed model-data comparisons have revealed the following main findings:

1. There is an overall agreement between model and data in the tides and the diurnal variations of ionospheric parameters (hmF_2 and NmF_2). The EIA crest is stronger in the winter hemisphere in the morning sector and gives way to the summer hemisphere in the afternoon sector. In spite of the general agreement of the spatial structures of NmF2, the model NmF2 is often lower than observations. At some locations, WACCM-X simulated NmF2 is almost half of the observation. hmF_2 is higher over the equator in the daytime and pre-midnight sector, whereas it is higher at middle latitudes in the post-midnight sector. Daytime upward ion drifts are seen in WACCM-X, TIE-GCM, and C/NOFS, but there are differences among them. For instance, model results (WACCM-X and TIE-GCM) are dominated by diurnal variations, whereas observations have more temporal variability over equator.

2. Complicated seasonal variations are seen in ionospheric NmF_2, hmF_2, and tidal components at middle and low latitudes in the deep solar minimum year of 2008. During daytime, equinoctial asymmetry and semiannual variations are present in both WACCM-X and COSMIC NmF_2. WACCM-X captures the peak of the DE3 temperature tide at June solstice well, whereas the additional peak of the DE3 temperature tide at the December Solstice is only seen in WACCM-X, but not in the SABER observations. There is a good consistency between WACCM-X and SABER SW2 temperature tidal components in terms of seasonal variations. Both of them maximize at the June solstice, with a secondary peak around the December solstice.

These comparisons give us confidence that WACCM-X can be a useful tool in studying the complex dynamics, electrodynamics, and chemical processes in the whole atmosphere system.

Acknowledgements

We acknowledge the CESM, CAM, WACCM, and WACCM-X development teams at NCAR and, in particular, Art Richmond, Ben Foster, and Francis Vitt for key contributions to WACCM-X. We would like to also acknowledge NASA grants NASA grants NNX13AE20G, NNX14AE06G, NNX14AF20G, NNX14AH54G, and NNX15AB83, and NSF grant 1135432, and AFOSR grant FA9550-16-1-0050. The TIDI and SABER datasets are obtained from http://timed.hao.ucar.edu/tidi/data.html and http://saber.gats-inc.com/, respectively. COSMIC electron density is available at http://cdaac-www.cosmic.ucar.edu/cdaac/products.html. WACCM-X and TIE-GCM are open-source community models; output from model runs used in this study are archived on the NCAR High Performance Storage System. NCAR is sponsored by the National Science Foundation.

References

Akmaev, R. A., and G. M. Shved (1980), Modelling of the composition of the lower thermosphere taking account of the dynamics with applications to tidal variations of the forbidden O I 5577 A airglow, Journal of Atmospheric and Terrestrial Physics, 42, 705–716.

Akmaev, R. A., T. J. Fuller-Rowell, F. Wu, J. M. Forbes, X. Zhang, A. F. Anghel, M. D. Iredell, S. Moorthi, and H.-M. Juang (2008), Tidal variability in the lower thermosphere: Comparison of Whole Atmosphere Model (WAM) simulations with observations from TIMED, Geophys. Res. Lett., 35, L03810, doi:10.1029/2007GL032584.

Akmaev, R. A. (2011), Whole atmosphere modeling: Connecting terrestrial and space weather, Rev. Geophys., 49, RG4004, doi:10.1029/2011RG000364.

Burns, A. G., S. C. Solomon, W. Wang, L. Qian, Y. Zhang, and L. J. Paxton (2012), Daytime climatology of ionospheric NmF2 and hmF2 from COSMIC data, J. Geophys. Res., 117, A09315, doi: 10.1029/2012JA017529.

Chapman, S., and R. S. Lindzen (1970), Atmospheric Tides: Thermal and Gravitational, 200 pp., Gordon and Breach, New York.

Cliver, E. W., Y. Kamide, and A. G. Ling (2000), Mountains versus valleys: Semiannual variation of geomagnetic activity, J. Geophys. Res., 105(A2), 2413–2424, doi:10.1029/1999JA900439.

Dickinson, R. E., E. C. Ridley, and R. G. Roble (1981), A three dimensional general circulation model of the thermosphere, J. Geophys. Res., 86, 1499–1512.

Fang, T.-W., R. A. Akmaev, R. A. Stoneback, T. Fuller-Rowell, H. Wang, and F. Wu (2016), Impact of midnight thermosphere dynamics on the equatorial ionospheric vertical drifts, J. Geophys. Res. Space Physics, 121, 4858–4868, doi:10.1002/2015JA022282.

Fejer, B. G., J. W. Jensen, and S.-Y. Su (2008), Quiet time equatorial F region vertical plasma drift model derived from ROCSAT-1 observations, J. Geophys. Res., 113, A05304, doi: 10.1029/2007JA012801.

Forbes, J. M., R. G. Roble, and C. G. Fesen (1993), Acceleration, heating, and compositional mixing of the thermosphere due to upward propagating tides, Journal of Geophysical Research: Space Physics, 98(A1), 311–321, doi:10.1029/92JA00442.

Fukao, S., M. D. Yamanaka, N. Ao, W. K. Hocking, T. Sato, M. Yamamoto, T. Nakamura, T. Tsuda, and S. Kato (1994), Seasonal variability of vertical eddy diffusivity in the middle atmosphere: 1. Three-year observations by the middle and upper atmosphere radar, J. Geophys. Res., 99, 18,973–18,987.

Fuller-Rowell, T. J. (1998), The “thermospheric spoon”: A mechanism for the semiannual density variation, J. Geophys. Res.,103, 3951–3956.

Fuller-Rowell, T. J., et al. (2008), Impact of terrestrial weather on the upper atmosphere, Geophys. Res. Lett., 35, L09808, doi:10.1029/2007GL032911.

Garcia, R.R., D.R. Marsh, D.E. Kinnison, B.A. Boville, and F. Sassi (2007), Simulation of secular trends in the middle atmosphere, 1950-2003. J. Geophys. Res., 112, doi: 10.1029/2006JD007485.

Gan Q., Du J., Ward W. E., Beagley S. R., Fomichev V. I., Zhang S. (2014) Climatology of the diurnal tides from eCMAM30 (1979 to 2010) and its comparisons with SABER, Earth Planets Space 66:103, doi: 10.1186/1880-5981-66-103.

Hagan, M. E., A. Maute, R. G. Roble, A. D. Richmond, T. J. Immel, and S. L. England (2007), Connections between deep tropical clouds and the Earth's ionosphere, Geophys. Res. Lett., 34, L20109, doi:10.1029/2007GL030142.

Hagan, M. E., and J. M. Forbes (2002), Migrating and nonmigrating diurnal tides in the middle and upper atmosphere excited by tropospheric latent heat release, J. Geophys. Res., 107(D24), 4754, doi: 10.1029/2001JD001236.

Hagan, M. E., and J. M. Forbes (2003), Migrating and nonmigrating semidiurnal tides in the upper atmosphere excited by tropospheric latent heat release, J. Geophys. Res., 108(A2), 1062, doi:10.1029/2002JA009466.

Heelis, R. A., J. K. Lowell and R. W. Spiro (1982), A model of the high-latitude ionosphere convection pattern, J. Geophys. Res., 87, 6339-6345.

Hurrell, J. W., M. M. Holland, P. R. Gent, S. Ghan, J. E. Kay, P. J. Kushner, J.-F. Lamarque, W. G. Large, D. Lawrence, K. Lindsay, W. H. Lipscomb, M. C. Long, N. Mahowald, D. R. Marsh, R. B. Neale, P. Rasch, S. Vavrus, M. Vertenstein, D. Bader, W. D. Collins, J. J. Hack, J. Kiehl, and S. Marshall (2013), The community earth system model: A framework for collaborative research, Bulletin of the American Meteorological Society, 94, 1339–1360, doi:10.1175/BAMS-D-12-00121.1.

Immel, T. J., E. Sagawa, S. L. England, S. B. Henderson, M. E. Hagan, S. B. Mende, H. U. Frey, C. M. Swenson, and L. J. Paxton (2006), Control of equatorial ionospheric morphology by atmospheric tides, Geophys. Res. Lett., 33, L15108, doi:10.1029/2006GL026161.

Jin, H., Miyoshi, Y., Fujiwara, H., Shinagawa, H. (2008), Electrodynamics of the formation of ionospheric wave number4 longitudinal structure, Journal of Geophysical Research 113, A09307, http://dx.doi.org/10.1029/2008JA013301.

Jin, H., Y. Miyoshi, H. Fujiwara, H. Shinagawa, K. Terada, N. Terada, M. Ishii, Y. Otsuka, and A. Saito (2011), Vertical connection from the tropospheric activities to the ionospheric longitudinal structure simulated by a new Earth's whole atmosphere-ionosphere coupled model, J. Geophys. Res., 116, A01316, doi:10.1029/2010JA015925.

Jones, M., Jr., J. T. Emmert, D. P. Drob, and D. E. Siskind (2017), Middle atmosphere dynamical sources of the semiannual oscillation in the thermosphere and ionosphere, Geophys. Res. Lett., 44, 12–21, doi:10.1002/2016GL071741.

Kazimirovsky, E.S., G.V. Vergasova (2009), Mesospheric, lower thermospheric dynamics and external forcing effects: a review. Indian J. Radio & Space Phys. 38, 7–36.

Kil, H., S.-J. Oh, L. J. Paxton, and T.-W. Fang (2009), High-resolution vertical E X B drift model derived from ROCSAT-1data, J. Geophys. Res., 114, A10314,doi:10.1029/2009JA014324.

Killeen, T. L., Q. Wu, S. C. Solomon, D. A. Ortland, W. R. Skinner, R. J. Niciejewski, and D. A. Gell (2006), TIMED Doppler Interferometer: Overview and recent results, J. Geophys. Res., 111, A10S01, doi:10.1029/2005JA011484.

Kinnison, D.E., et al. (2007), Sensitivity of chemical tracers to meteorological parameters in the MOZART-3 chemical transport model, J. Geophys. Res., 112, D20302, doi: 10.1029/2006JD007879.

Kirchhoff, V. W. J. H., and B. R. Clemesha (1983), Eddy diffusion coefficients in the lower thermosphere, J. Geophys. Res., 88, 5765–5768.

Lastovicka, J. (2006), Forcing of the ionosphere by waves from below, J. Atmos. Sol. Terr. Phys., 68, 479–497.

Lei, J., et al. (2007), Comparison of COSMIC ionospheric measurements with ground-based observations and model predictions: Preliminary results, J. Geophys. Res., 112, A07308, doi:10.1029/2006JA012240.

Lieberman R. S., Ortland D. A., Yarosh E. S. (2003), Climatology and interannual variability of diurnal water vapor heating. J Geophys Res-Atmos 108(D3): doi: 10.1029/2002jd002308.

Lieberman R. S., Ortland D. A., Riggin D. M., Wu Q., Jacobi C. (2010), Momentum budget of the migrating diurnal tide in the mesosphere and lower thermosphere. J Geophys Res-Atmos 115: doi:10.1029/2009jd013684.

Lin, C. H., J. Y. Liu, T. W. Fang, P. Y. Chang, H. F. Tsai, C. H. Chen, and C. C. Hsiao (2007), Motions of the equatorial ionization anomaly crests imaged by FORMOSAT-3/COSMIC, Geophys. Res. Lett., 34, L19101, doi:10.1029/2007GL030741.

Liu, H.-L. (2016), Variability and predictability of the space environment as related to lower atmosphere forcing, Space Weather, 14, doi:10.1002/2016SW001450.

Liu, H.-L. et al. (2010), Thermosphere extension of the Whole Atmosphere Community Climate Model, J. Geophys. Res., 115, A12302, doi: 10.1029/2010JA015586.

Liu, H.-L., and R. G. Roble (2002), A study of a self-generated stratospheric sudden warming and its mesospheric-lower thermospheric impacts using the coupled TIME-GCM/CCM3, J. Geophys. Res., 107(D23), 4695, doi:10.1029/2001JD001533.

Liu, H. -L. and co-authors (2018), Development and Validation of the Whole Atmosphere Community Climate Model with Thermosphere and Ionosphere Extension (WACCM-X), doi: 10.1002/2017MS001232, JAMES.

Liu, L., B. Zhao, W. Wan, B. Ning, M. L. Zhang, and M. He (2009), Seasonal variations of the ionospheric electron densities retrieved from Constellation Observing System for Meteorology, Ionosphere, and Climate mission radio occultation measurements, J. Geophys. Res., 114, A02302, doi: 10.1029/2008JA013819.

Liu, J., L. Liu, B. Zhao, and W. Wan (2012), Influence of interplanetary solar wind sector polarity on the ionosphere, J. Geophys. Res., 117, A08335, doi: 10.1029/2012JA017859.

Liu, J., L. Liu, B. Zhao, Y. Wei, L. Hu, and B. Xiong (2012), High-speed stream impacts on the equatorial ionization anomaly region during the deep solar minimum year 2008, J. Geophys. Res., 117, A10304, doi:10.1029/2012JA018015.

Liu J., Wenbin Wang, Alan Burns, Libo Liu and Joe McInerney (2017), A TIEGCM Numerical Study of the Source and Evolution of Ionospheric F-region Tongues of Ionization: Universal Time and Interplanetary Magnetic Field Dependence, Journal of Atmospheric and Solar-Terrestrial Physics, http://dx.doi.org/10.1016/j.jastp.2017.03.005.

Maeda, S., T. J. Fuller-Rowell, and D. S. Evans (1989), Zonally averaged dynamical and compositional response of the thermosphere to auroral activity during September 18–24, 1984, J. Geophys. Res., 94, 16,869–16,883.

Maute, A., Thermosphere-Ionosphere-Electrodynamics General Circulation Model for the Ionospheric Connection Explorer: TIEGCM-ICON, Space Sci Rev (2017). doi:10.1007/s11214-017-0330-3.

Marsh, D. R., M.J. Mills, D.E. Kinnison, J.-F. Lamarque, N. Calvo, and L. M. Polvani (2013), Climate change from 1850 to 2005 simulated in CESM1(WACCM), Journal of Climate, 26, doi:10.1175/JCLI-D-12-00558.1.

McLandress C (2002), The seasonal variation of the propagating diurnal tide in the mesosphere and lower thermosphere. Part II: The role of tidal heating and zonal mean winds. J. Atmos. Sci. 59(5): 907–922, doi: 10.1175/1520-0469.

Mertens, C. J., et al. (2004), SABER observations of mesospheric temperatures and comparisons with falling sphere measurements taken during the 2002 summer MaCWAVE campaign, Geophys. Res. Lett., 31, L0310 5, doi:10.1029/2003GL018605.

Miyoshi, Y., and H. Fujiwara (2003), Day-to-day variations of migrating diurnal tide simulated by a GCM from the ground surface to the exobase, Geophys. Res. Lett., 30(15), 1789, doi:10.1029/2003GL017695.

Millward, G. H., R. J. Moffett, S. Quegan, and T. J. Fuller-Rowell (1996), Ionospheric F2 layer seasonal and semiannual variations, J. Geophys. Res., 101, 5149–5156, doi:10.1029/95JA03343.

Oberheide, J., J. M. Forbes, K. Häusler, Q. Wu, and S. L. Bruinsma (2009), Tropospheric tides from 80 to 400 km: Propagation, interannual variability, and solar cycle effects, J. Geophys. Res., 114, D00I05, doi:10.1029/2009JD012388.

Pedatella, N. M., K. Raeder, J. L. Anderson, and H. -L. Liu (2013), Application of data assimilation in the Whole Atmosphere Community Climate Model to the study of day-to-day variability in the middle and upper atmosphere, Geophys. Res. Lett., 40, 4469–4474, doi:10.1002/grl.50884.

Qian, L., S. C. Solomon, and T. J. Kane (2009), Seasonal variation of thermospheric density and composition, J. Geophys. Res., 114, A01312, doi:10.1029/2008JA013643.

Qian, L., A. G. Burns, S. C. Solomon, and W. Wang (2013), Annual/semiannual variation of the ionosphere, Geophys. Res. Lett., 40,1928–1933, doi:10.1002/grl.50448.

Qian, L., A. G. Burns, B. A. Emery, B. Foster, G. Lu, A. Maute, A. D. Richmond, R. G. Roble, S. C. Solomon, and W. Wang (2014), The NCAR TIE-GCM: A community model of the coupled thermosphere/ionosphere system, in Modeling the Ionosphere-Thermosphere System, J. Huba, R. Schunk, and G. Khazanov, eds., AGU Geophysical Monograph Series, 201, 73, doi:10.1002/9781118704417.ch7.

Qian, L., and J. Yue (2017), Impact of the lower thermospheric winter-to-summer residual circulation on thermospheric composition, Geophys. Res. Lett., 44, doi:10.1002/2017GL073361.

Ren, Z., Wan, W., Xiong, J., Liu, L. (2010), Simulated wave number 4 structure in equatorial F-region vertical plasma drifts. Journal of Geophysical Research 115, A05301, http://dx.doi.org/10.1029/2009JA014746.

Remsberg, E. E., et al. (2008), Assessment of the quality of the Version 1.07 temperature-versus-pressure profiles of the middle atmosphere from TIMED/SABER, J. Geophys. Res., 113, D17101, doi: 10.1029/2008JD010013.

Richter, J.H., F. Sassi and R.R. Garcia (2010). Toward a physically based gravity wave source parameterization in a General Circulation Model., J. Atmos. Sci., 67 (1), 136-156, doi:10.1175/2009JAS3112.1.

Rienecker et al. (2011), MERRA: NASA’s Modern-Era Retrospective Analysis for Research and Applications, J. Climate, 24, 3624-3648, doi:10.1175/JCLI-D-11-00015.1

Rishbeth, H. (1998), How the thermospheric circulation affects the ionospheric F2-layer, J. Atmos. Sol. Terr. Phys., 60, 1385–1402.

Rishbeth, H. (2000), The equatorial F-layer: Progress and puzzles, Ann. Geophys., 18, 730.

Roble, R. G., R. E. Dickinson, and E. C. Ridley (1982), Global circulation and temperature structure of thermosphere with high-latitude plasma convection, J. Geophys. Res., 87, 1599–1614.

Roble, R. G., and E. C. Ridley (1987), An auroral model for the NCAR thermosphere general circulation model (TGCM), Ann. Geophys., 5A, 369-382.

Roble, R. G., and E. C. Ridley (1994), A thermosphere-ionosphere- mesosphere-electrodynamics general circulation model (time-GCM), Geophys. Res. Lett., 21, 417–420.

Roble, R.G. (2000), On the Feasibility of Developing a Global Atmospheric Model Extending from the Ground to the Exosphere, in Atmospheric Science Across the Stratopause (eds D. E. Siskind, S. D. Eckermann and M. E. Summers), American Geophysical Union, Washington, D. C.. doi: 10.1029/GM123p0053.

Sasi, M. N., and L. Vijayan (2001), Turbulence characteristics in the tropical mesosphere as obtained by MST radar at Gadanki (13.5°N, 79.2°E), Ann. Geophys., 19, 1019–1025.

Sagawa, E., Immel, T.J., Frey, H.U., Mende, S.B. (2005), Longitudinal structure of the equatorial anomaly in the nighttime ionosphere observed by IMAGE/FUV, Journal of Geophysical Research 110, A11302, http://dx.doi.org/10.1029/ 2004JA010848.

Scherliess, L., and B. G. Fejer (1999), Radar and satellite global equatorial F region vertical drift model, J. Geophys. Res., 104(A4), 6829-6842, doi: 10.1029/1999JA900025.

Schreiner, W. S., S. V. Sokolovskiy, C. Rocken, and D. C. Hunt, (1999), Analysis and validation of GPS/MET radio occultation data in the ionosphere. Radio Sci., 34(4), 949-966, doi: 10.1029/1999RS900034.

Solomon, S. C., L. Qian, and A. G. Burns (2013), The anomalous ionosphere between solar cycles 23 and 24, J. Geophys. Res. Space Physics, 118, 6524, doi:10.1002/jgra.50561.

Stoneback, R. A., R. A. Heelis, A. G. Burrell, W. R. Coley, B. G. Fejer, and E. Pacheco (2011), Observations of quiet time vertical ion drift in the equatorial ionosphere during the solar minimum period of 2009, J. Geophys. Res., 116, A12327, doi: 10.1029/2011JA016712.

Strom, S. R. and G. Iwanaga (2005), Overview and History of the Defense Meteorological Satellite Program, Crosslink, The Aerospace Corporation magazine of advances in aerospace technology, Vol. 6, No 1.

Su, S.-Y., C. K. Chao, and C. H. Liu (2008), On monthly/seasonal/longitudinal variations of equatorial irregularity occurrences and their relationship with the postsunset vertical drift velocities, J. Geophys. Res., 113, A05307, doi:10.1029/2007JA012809.

Sutton, E. K., J. P. Thayer, W. Wang, S. C. Solomon, X. Liu, and B. T. Foster (2015), A self-consistent model of helium in the thermosphere, J. Geophys. Res. Space Physics, 120, 6884–6900, doi:10.1002/2015JA021223.

Wan, W., Z. Ren, F. Ding, J. Xiong, L. Liu, B. Ning, B. Zhao, G. Li, and M. -L. Zhang (2012), A simulation study for the couplings between DE3 tide and longitudinal WN4 structure in the thermosphere and ionosphere, J. Atmos. Sol. Terr. Phys., 90-91, 52–60, doi: 10.1016/j.jastp.2012.04.011.

Wu, Q., D. A. Ortland, T. L. Killeen, R. G. Roble, M. E. Hagan, H.-L. Liu, S. C. Solomon, J. Xu, W. R. Skinner, and R. J. Niciejewski (2008), Global distribution and interannual variations of mesospheric and lower thermospheric neutral wind diurnal tide:1. Migrating tide, J. Geophys. Res., 113, A05308, doi: 10.1029/2007JA012542.

Wu, Q., D. A. Ortland, B. Foster, and R. G. Roble (2012), Simulation of nonmigrating tide influences on the thermosphere and ionosphere with a TIMED data driven TIEGCM, J. Atmos. Sol. Terr. Phys., 90-91, 61–67, doi: 10.1016/j.jastp.2012.02.009.

Xu J. Y., Smith AK, Liu HL, Yuan W, Wu Q, Jiang GY, Mlynczak MG, Russell JM, Franke SJ (2009), Seasonal and quasi-biennial variations in the migrating diurnal tide observed by Thermosphere, Ionosphere, Mesosphere, Energetics and Dynamics (TIMED). J Geophys Res-Atmos 114: doi: 10.1029/2008jd011298.

Yamazaki, Y., and A. D. Richmond (2013), A theory of ionospheric response to upward-propagating tides: Electrodynamic effects and tidal mixing effects, J. Geophys. Res. Space Physics, 118, 5891–5905, doi: 10.1002/jgra.50487.

Yue, J., and W. Wang (2014), Changes of thermospheric composition and ionospheric density caused by quasi two-day wave dissipation, J. Geophys. Res. Space Physics, 119, 2069–2078, doi:10.1002/2013JA019725.

Yue, X., W. S. Schreiner, J. Lei, S. V. Sokolovskiy, C. Rocken, D. C. Hunt, and Y.-H. Kuo (2010), Error analysis of Abel retrieved electron density profiles from radio-occultation measurements, Ann. Geophys., 28, 217–222.

Zhang, S.-R., Z. Chen, A. J. Coster, P. J. Erickson, and J. C. Foster (2013), Ionospheric symmetry caused by geomagnetic declination over North America, Geophys. Res. Lett., 40, 1-5, doi:10.1002/2013GL057933.

Zhang X. L., Forbes JM, Hagan ME, Russell JM, Palo SE, Mertens CJ, Mlynczak MG (2006), Monthly tidal temperatures 20–120 km from TIMED/SABER. J Geophys Res 111(A10): doi: 10.1029/2005ja011504.

Figures

Figure 1. Comparisons of hmF_2 (in units of km) between WACCM-X, COSMIC, and TIE-GCM at March Equinox.

Figure 2. The same as Figure 1 but at June Solstice.

Figure 3. Comparisons of NmF_2 (in units of m^{-3}) between WACCM-X, COSMIC, and TIE-GCM at March Equinox.

Figure 4. The same as Figure 3 but at June Solstice.

Figure 5. (a) Ionosphere NmF_2 (in units of m^{-3}) and (c) hmF_2 (in units of km) measured by the ionosonde at Jicamarca (12°S, 283°W, 1°N geomagnetic latitude) during days 300-320 in 2008. Scatter plots between observations (black line) and WACCM-X (red line) of (b) NmF2 and (d) hmF2 during days 60-366 in 2008. The correlation coefficients are given in Figures 5b and 5d.

Figure 6. The same as Figure 5, but for Boulder (40.0^{o} N, 254.7^{o} W, 48.9^{o} geomagnetic latitude).

Figure 7. Comparisons of vertical ion drifts (in units of m/s) over Jicamarca (12^{o} S, 76.8^{o} W) between WACCM-X (red solid line), TIE-GCM (red dashed line), Fejer-Scherliess empirical model (blue line), and C/NOFS observations (black cross).

Figure 8. Latitude-altitude cross-sections of temperature amplitude (in Kelvin) and zonal wind amplitude (in m/s) of DW1 in March from WACCM-X (left panels), SABER (right left) and TIDI (bottom right) observations.

Figure 9. The same as Figure 8 but for SW2.

Figure 10. The same as Figure 8 but for DE3.

Figure 11. Seasonal variations of temperature amplitude (in Kelvin) of DW1 at 95 km, DE3 at 110 km, and SW2 at 105 km from WACCM-X (left panel) and SABER observations (right panel).

Figure 12. Seasonal variations of climatological NmF_2, hmF_2, vertical drift (m/s), O/N_2, meridional wind (m/s), eddy diffusion coefficient (Kzz) from WACCM-X (left panel) and SABER observations (right panel) on the dayside (09-15 LT). Vertical Drift, O/N_2, Meridional wind are shown at 300 km, while Kzz is shown at 110 km.

Figure1.

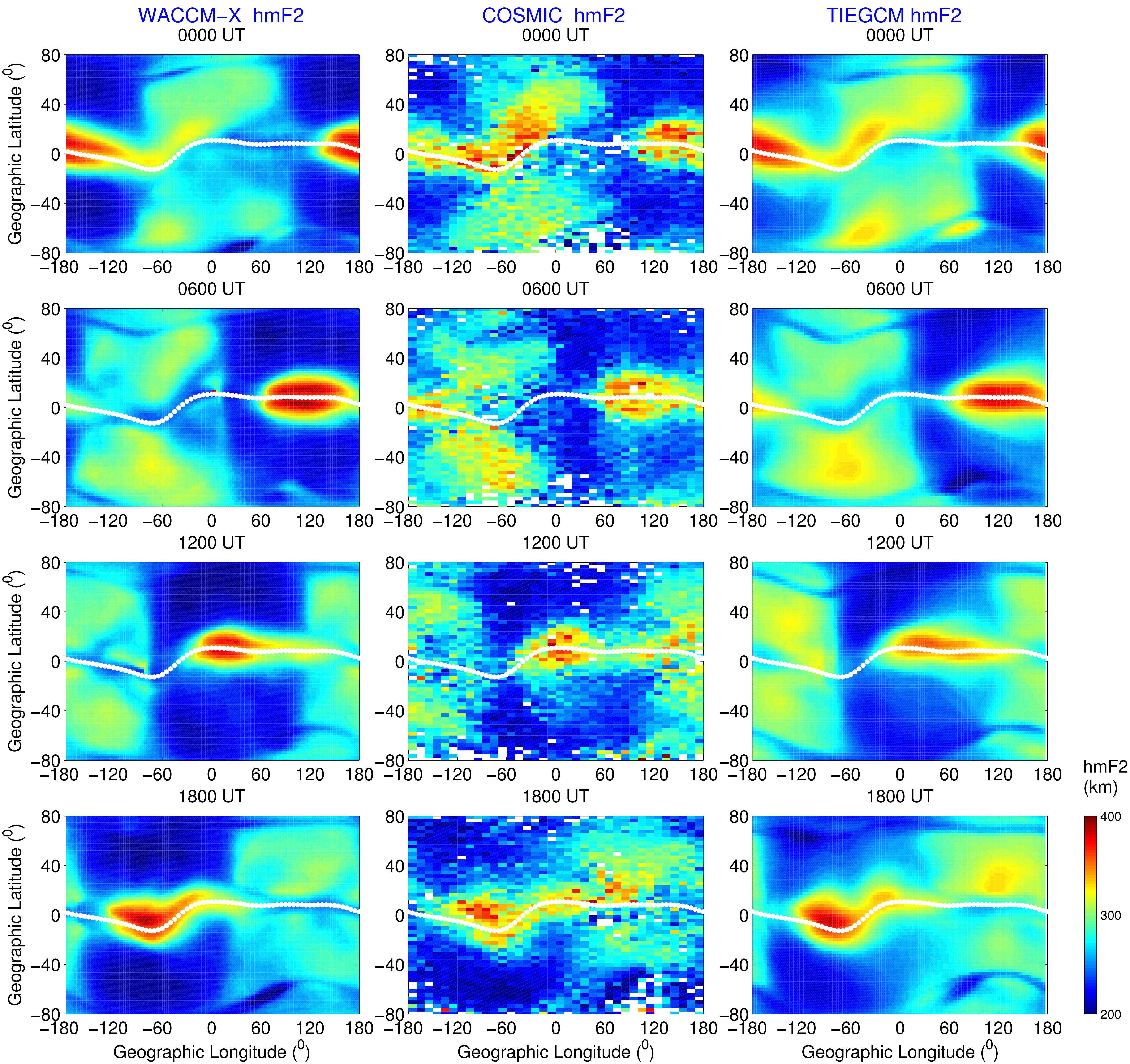
WACCM−X hmF2
COSMIC hmF2
TIEGCM hmF2
0000 UT
0600 UT
1200 UT
1800 UT
Geographic Latitude (^{0})
Geographic Longitude (^{0})
hmF2
(km)
400
300
200

Figure2.

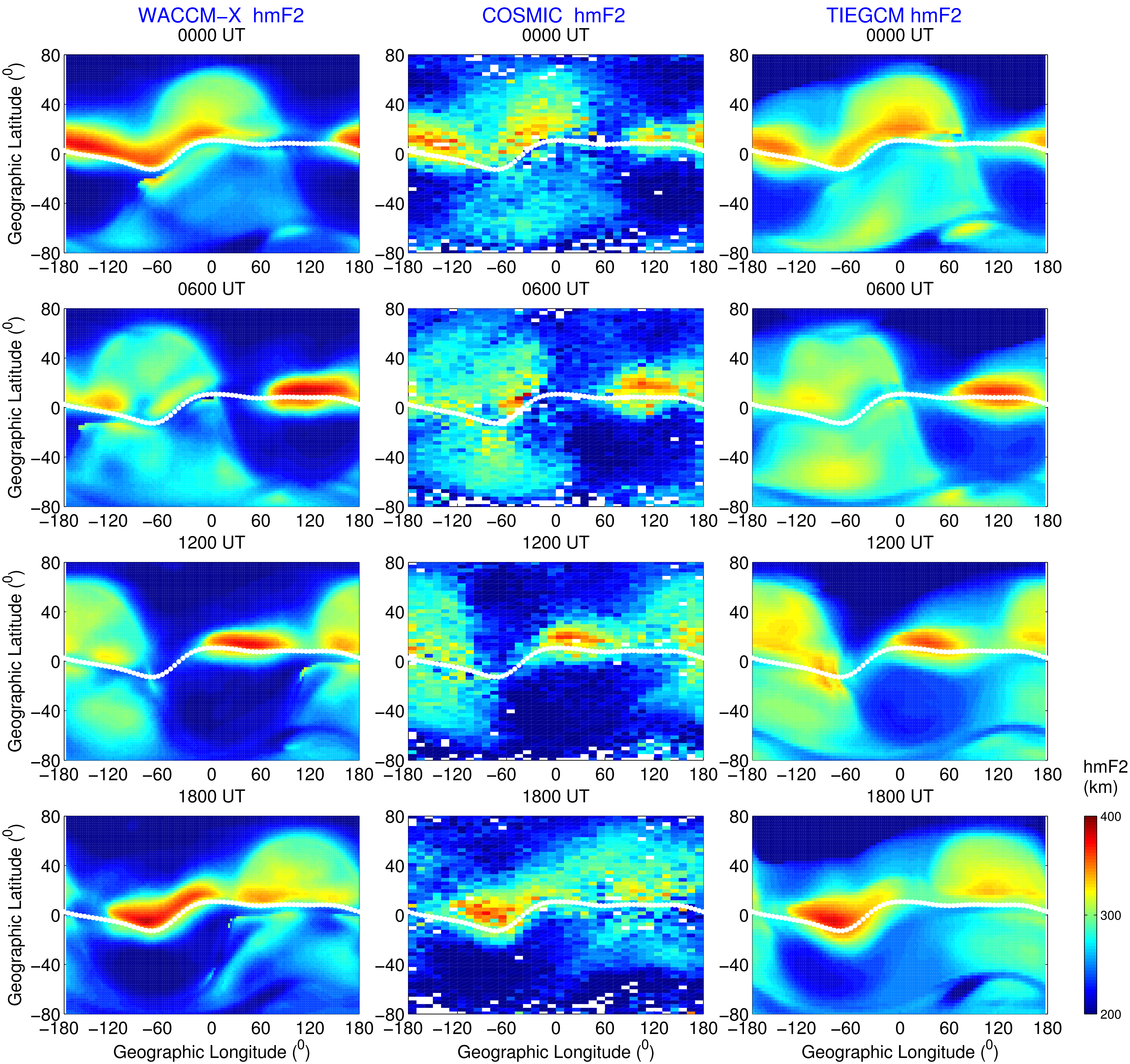

WACCM−X hmF2
COSMIC hmF2
TIEGCM hmF2
0000 UT
0600 UT
1200 UT
1800 UT
Geographic Latitude (^{0})
Geographic Longitude (^{0})
hmF2
(km)
400
300
200

Figure3.

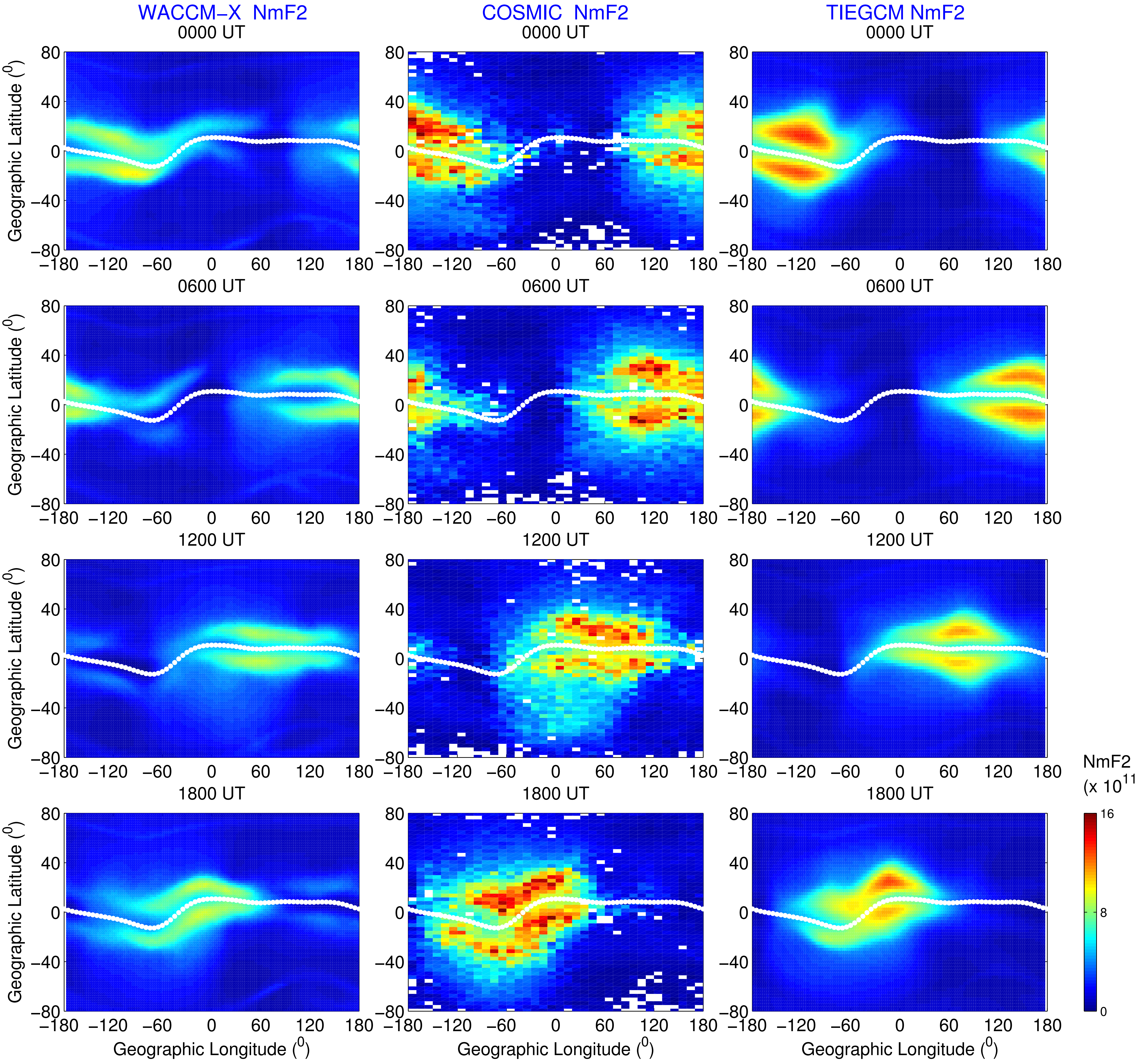

WACCM−X NmF2
COSMIC NmF2
TIEGCM NmF2
0000 UT
0600 UT
1200 UT
1800 UT
Geographic Latitude (^{0})
Geographic Longitude (^{0})
80
40
0
−40
−80
−180
−120
−60
0
60
120
180
NmF2
(x 10^{11})
16
8
0

Figure4.

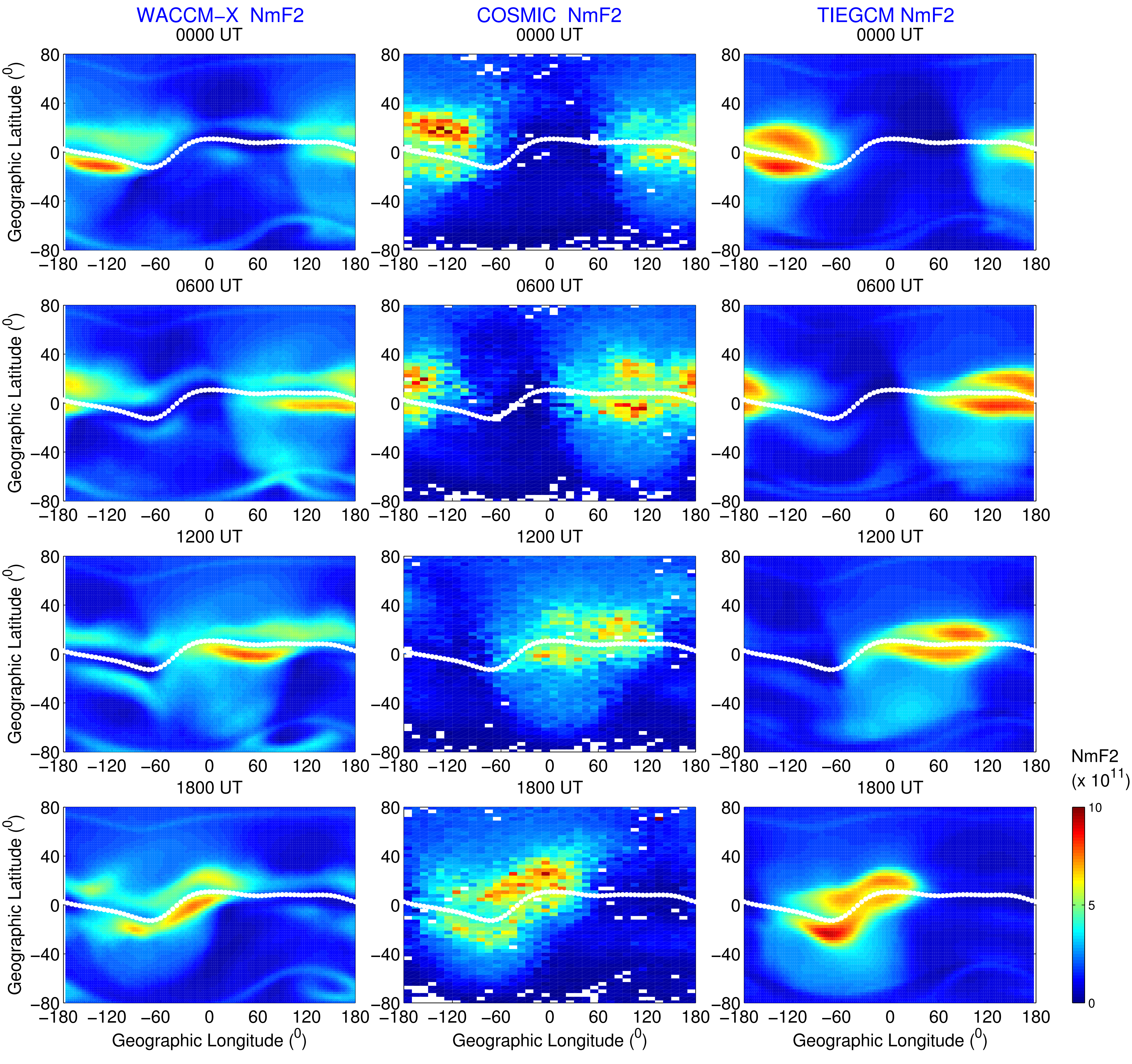

WACCM−X NmF2
COSMIC NmF2
TIEGCM NmF2
0000 UT
0600 UT
1200 UT
1800 UT
Geographic Latitude (0)
Geographic Longitude (0)
80
40
0
−40
−80
−180
−120
−60
0
60
120
180
NmF2
(x 10^11)
10
5
0

Figure5.

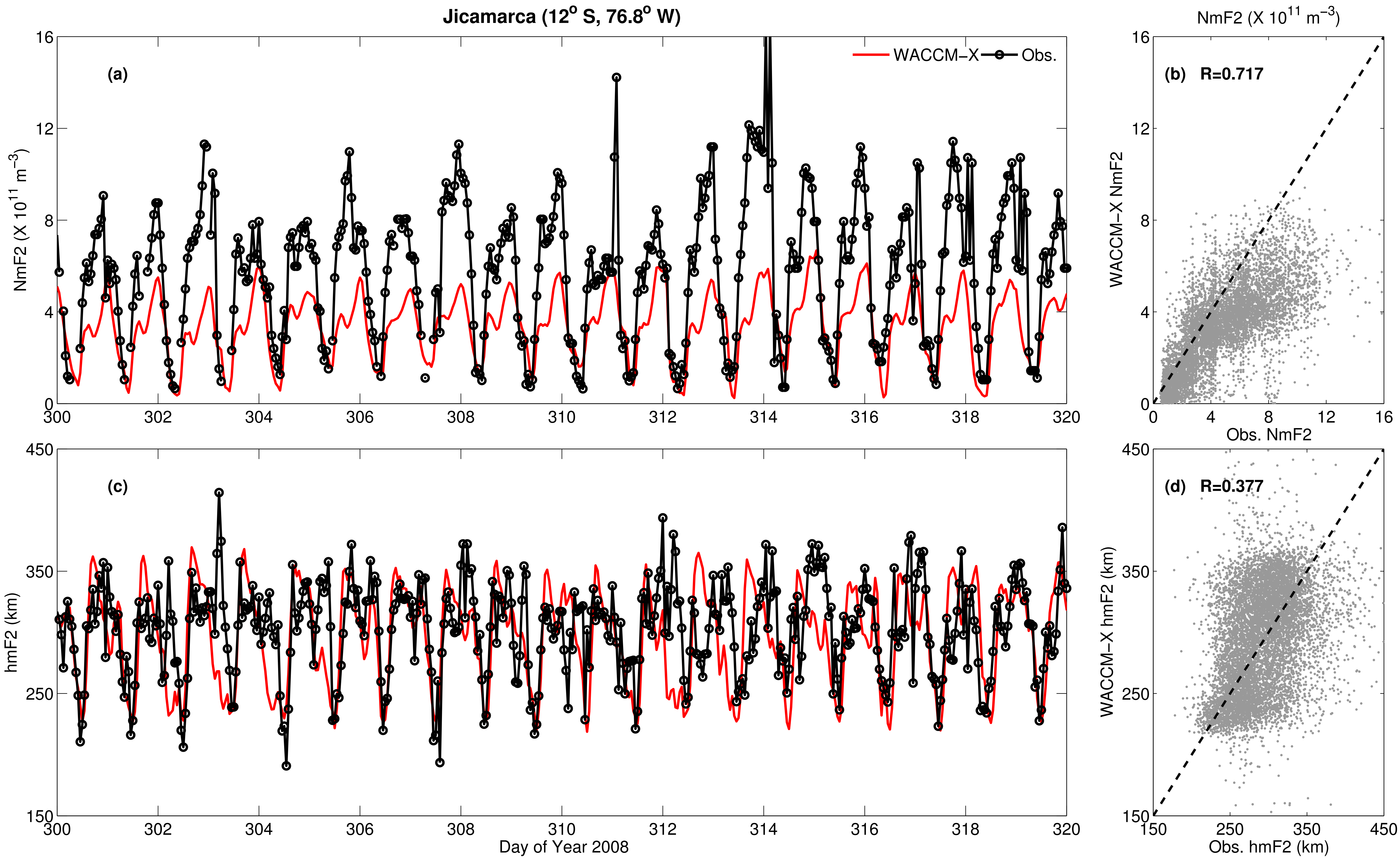

Jicamarca (12° S, 76.8° W)
NmF2 (X 10^11 m^-3)
WACCM−X
Obs.
(a)
(b) R=0.717
(c)
(d) R=0.377
NmF2 (X 10^11 m^-3)
WACCM−X NmF2
Obs. NmF2
hmF2 (km)
WACCM−X hmF2 (km)
Obs. hmF2 (km)
Day of Year 2008

Figure6.

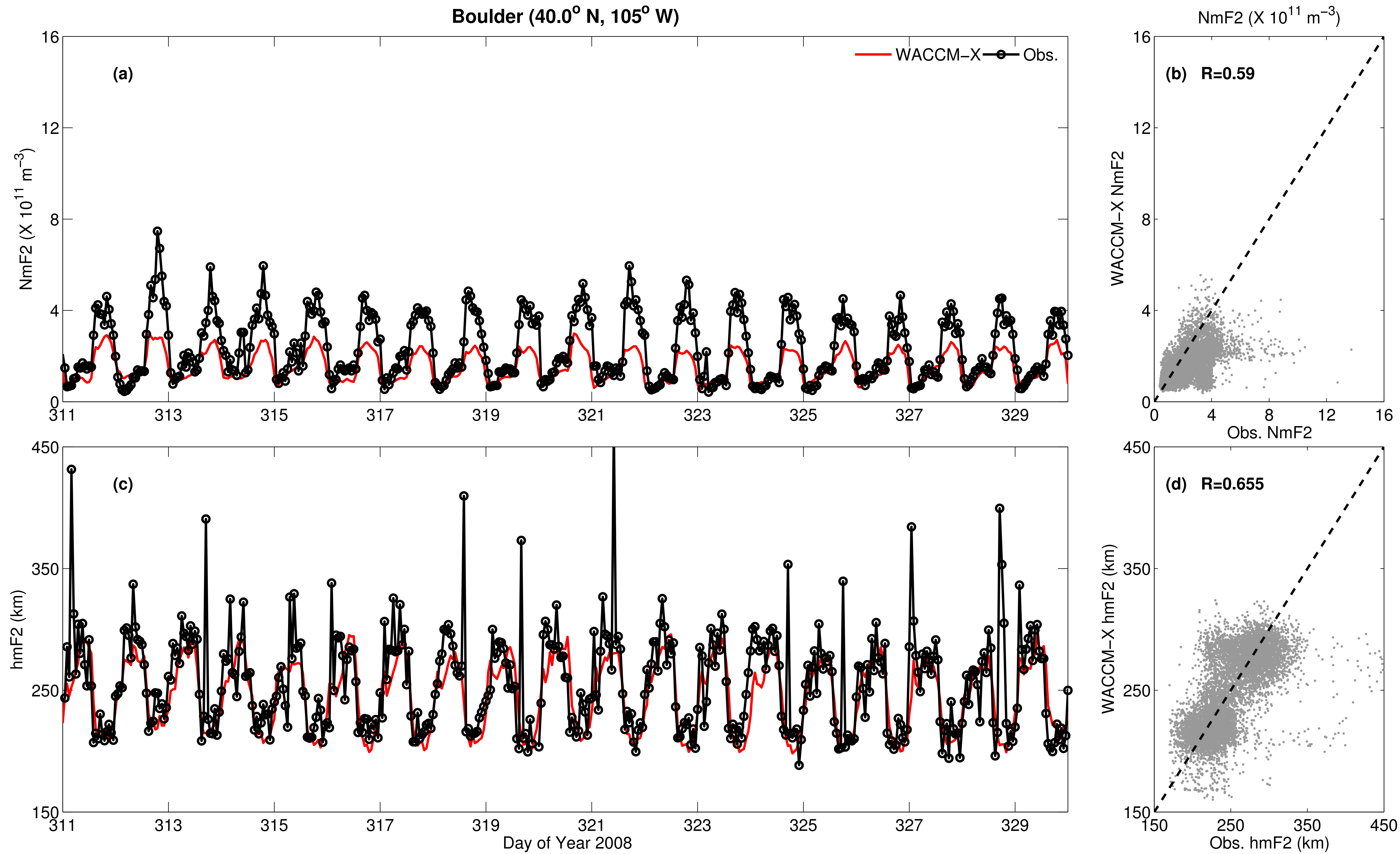
Boulder (40.0° N, 105° W)
NmF2 (X 10^11 m^-3)
(a)
WACCM−X
Obs.
NmF2 (X 10^11 m^-3)
(b) R=0.59
WACCM−X NmF2
Obs. NmF2
(c)
hmF2 (km)
Day of Year 2008
(d) R=0.655
WACCM−X hmF2 (km)
Obs. hmF2 (km)

Figure7.

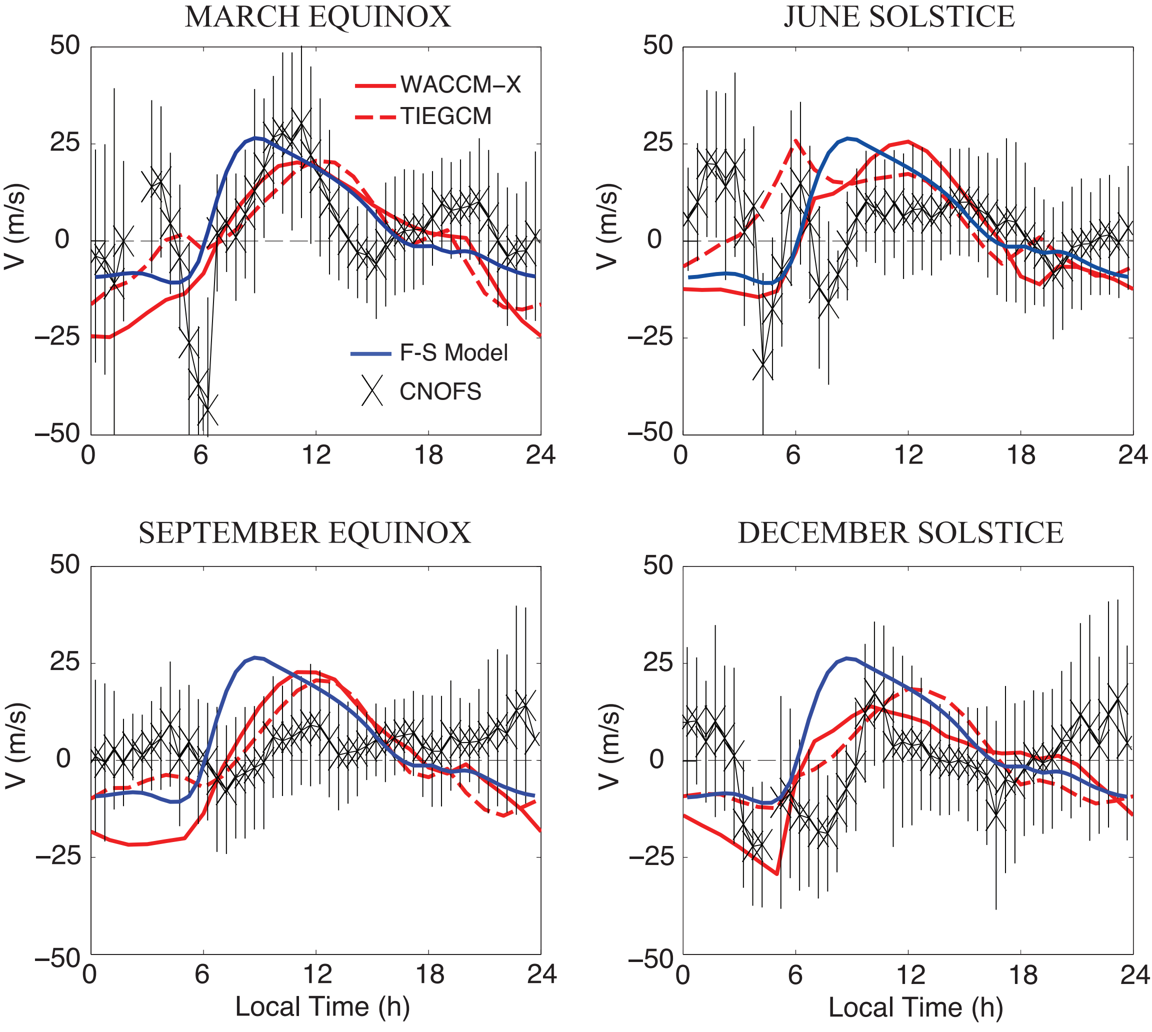
MARCH EQUINOX
JUNE SOLSTICE
SEPTEMBER EQUINOX
DECEMBER SOLSTICE
WACCM−X
TIEGCM
F-S Model
CNOFS
V (m/s)
Local Time (h)
50
25
0
−25
−50
0
6
12
18
24

Figure8.

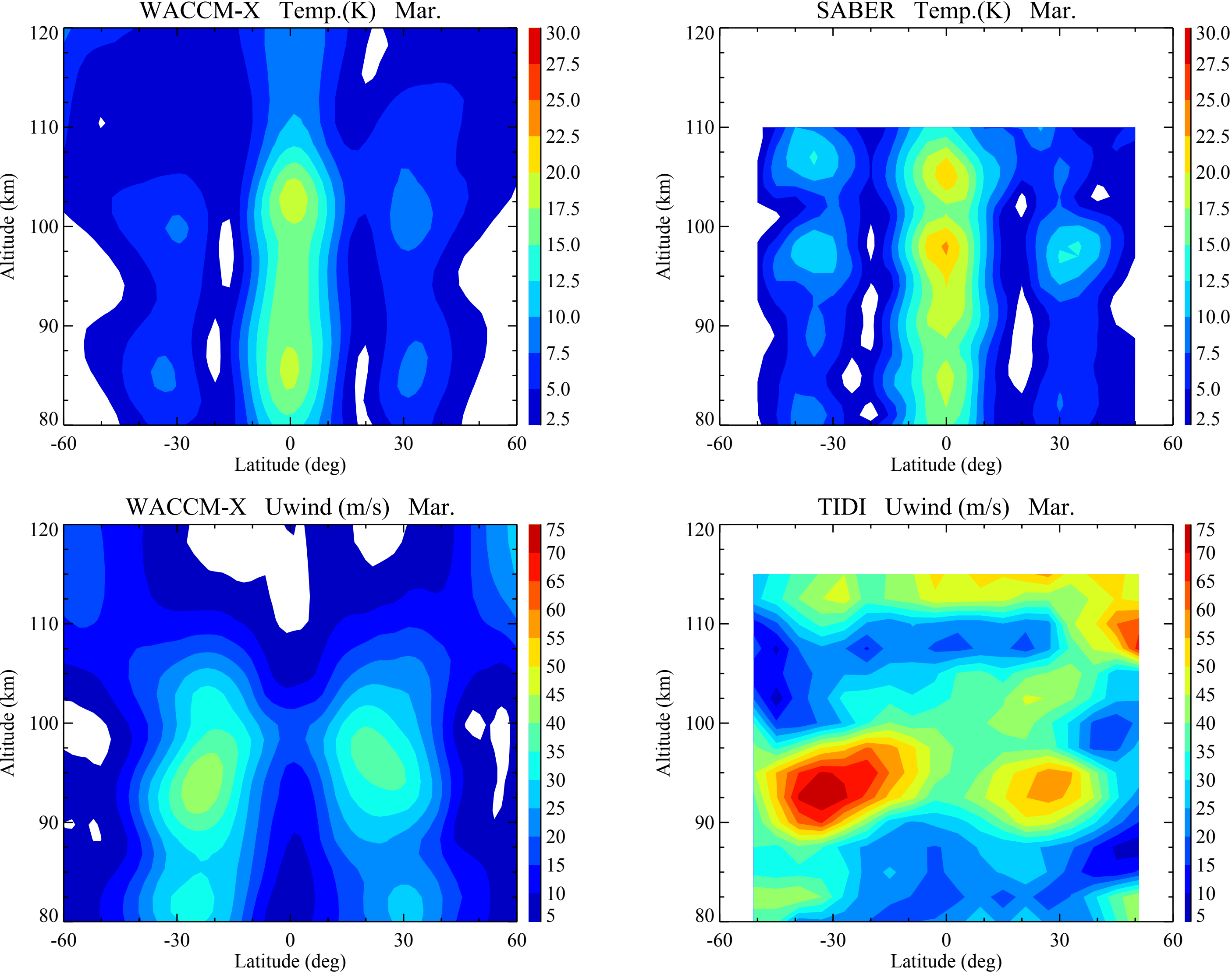

WACCM-X Temp.(K) Mar.
SABER Temp.(K) Mar.
WACCM-X Uwind (m/s) Mar.
TIDI Uwind (m/s) Mar.
Altitude (km)
Latitude (deg)
120
110
100
90
80
-60
-30
0
30
60
30.0
27.5
25.0
22.5
20.0
17.5
15.0
12.5
10.0
7.5
5.0
2.5
75
70
65
60
55
50
45
40
35
30
25
20
15
10
5

Figure9.

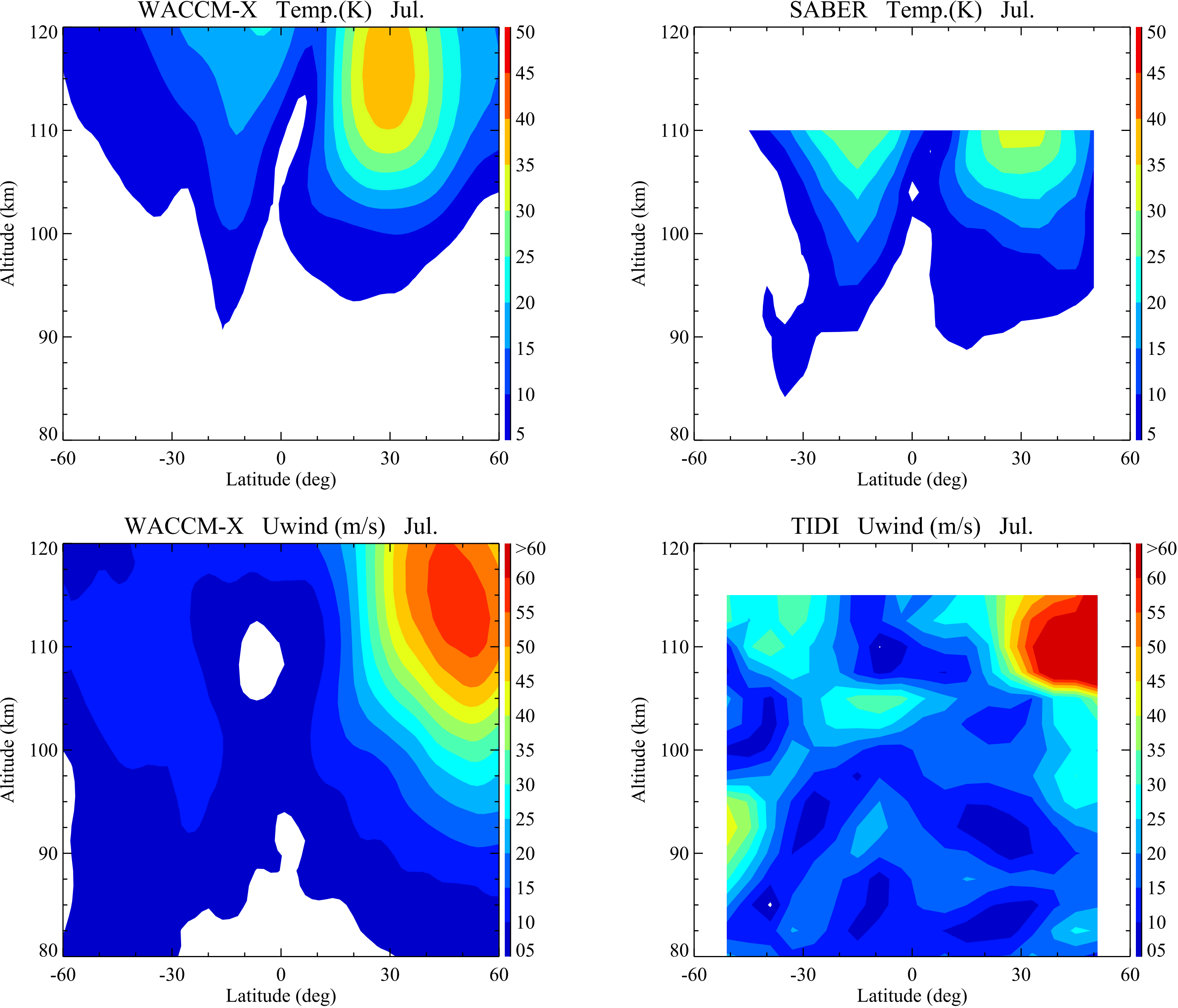
WACCM-X Temp.(K) Jul.
SABER Temp.(K) Jul.
WACCM-X Uwind (m/s) Jul.
TIDI Uwind (m/s) Jul.
Altitude (km)
Latitude (deg)
120
110
100
90
80
-60
-30
0
30
60
50
45
40
35
30
25
20
15
10
5
>60
05

Figure10.

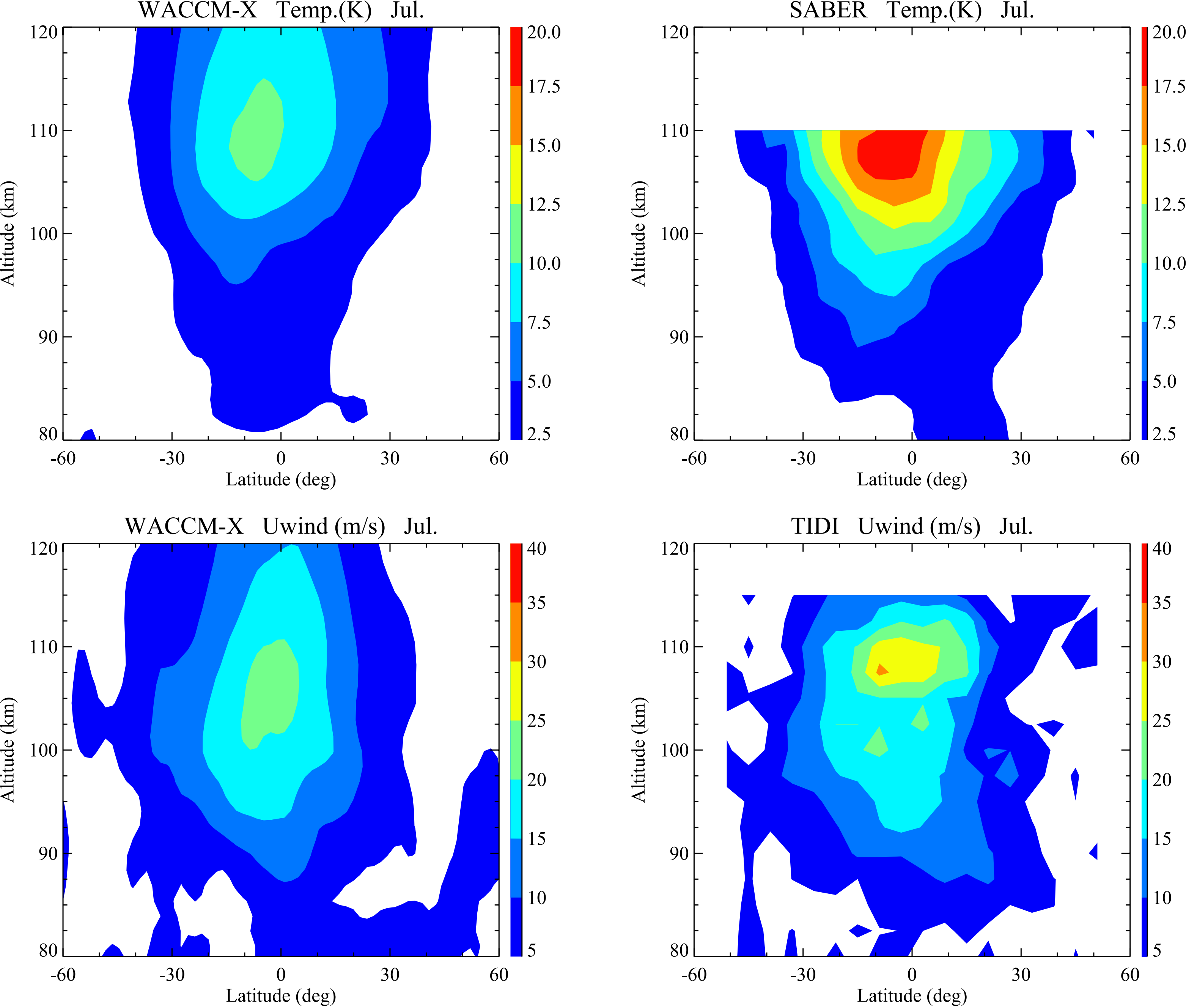
WACCM-X Temp.(K) Jul.
SABER Temp.(K) Jul.
WACCM-X Uwind (m/s) Jul.
TIDI Uwind (m/s) Jul.
Altitude (km)
Latitude (deg)
-60
-30
0
30
60
80
90
100
110
120
2.5
5.0
7.5
10.0
12.5
15.0
17.5
20.0
5
10
15
20
25
30
35
40

Figure11.

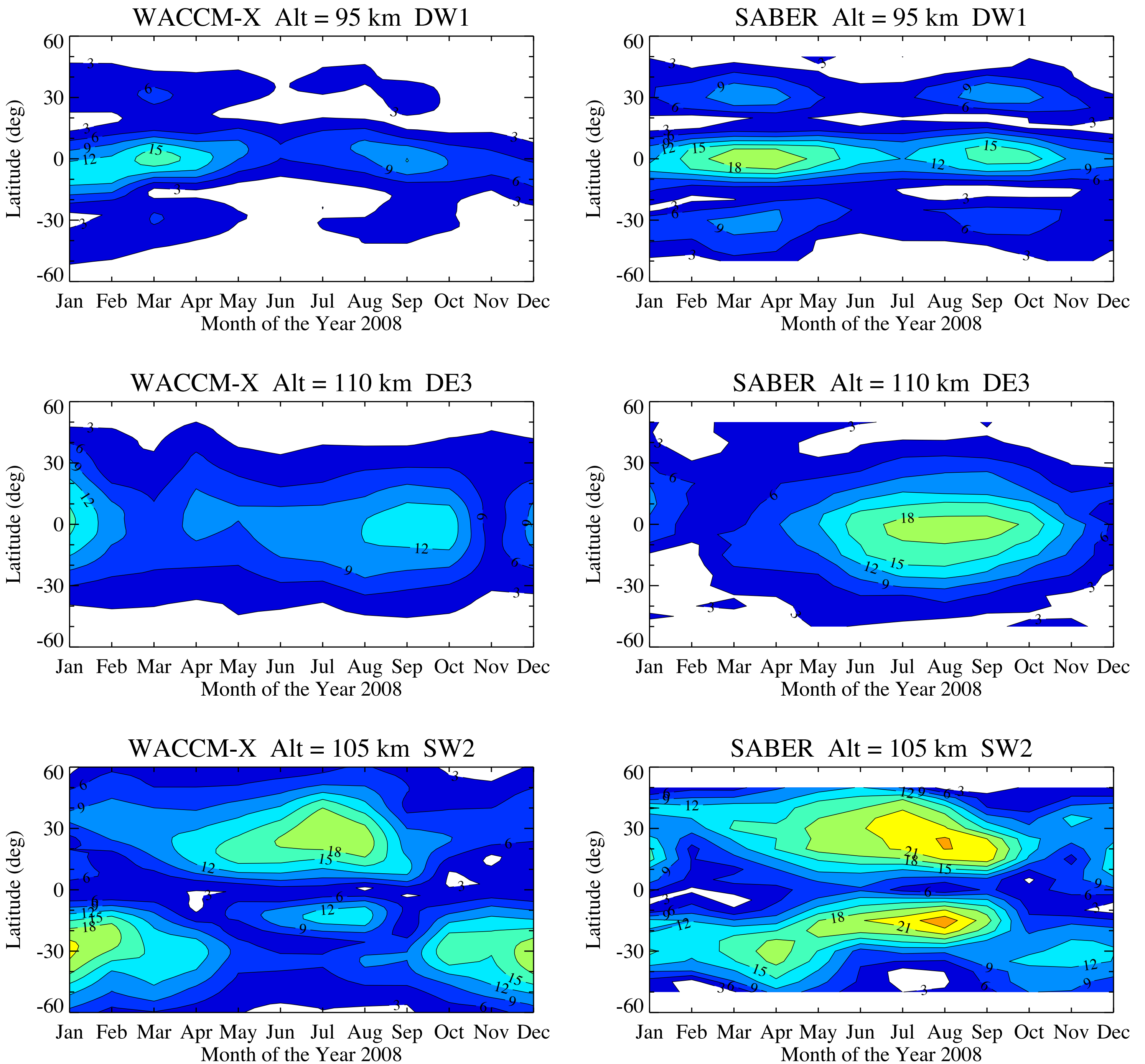
WACCM-X Alt = 95 km DW1
SABER Alt = 95 km DW1
WACCM-X Alt = 110 km DE3
SABER Alt = 110 km DE3
WACCM-X Alt = 105 km SW2
SABER Alt = 105 km SW2
Latitude (deg)
Month of the Year 2008
Jan Feb Mar Apr May Jun Jul Aug Sep Oct Nov Dec
60 30 0 -30 -60

Figure12.

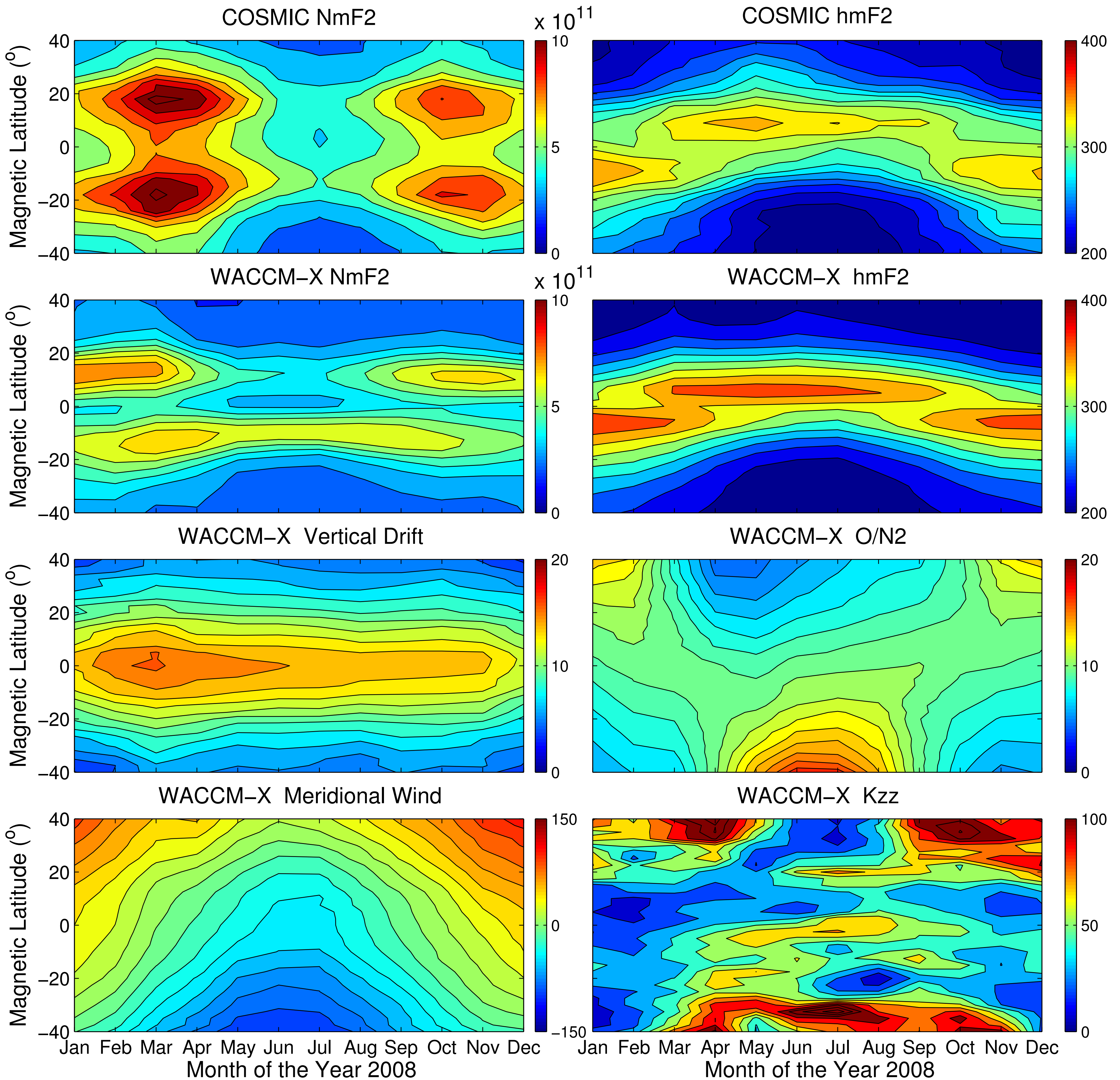

COSMIC NmF2
x 10^11
COSMIC hmF2
WACCM−X NmF2
x 10^11
WACCM−X hmF2
WACCM−X Vertical Drift
WACCM−X O/N2
WACCM−X Meridional Wind
WACCM−X Kzz
Magnetic Latitude (°)
40
20
0
−20
−40
10
5
0
400
300
200
20
10
0
150
0
−150
100
50
0
Jan Feb Mar Apr May Jun Jul Aug Sep Oct Nov Dec
Month of the Year 2008